

Wind and Temperature Retrievals in the 17 May 1981 Arcadia, Oklahoma, Supercell: Ensemble Kalman Filter Experiments

DAVID C. DOWELL

Advanced Study Program, National Center for Atmospheric Research, Boulder, Colorado*

FUQING ZHANG

Department of Atmospheric Sciences, Texas A&M University, College Station, Texas

LOUIS J. WICKER

National Severe Storms Laboratory, Norman, Oklahoma

CHRIS SNYDER AND N. ANDREW CROOK

National Center for Atmospheric Research, Boulder, Colorado*

(Manuscript received 14 October 2003, in final form 5 February 2004)

ABSTRACT

The feasibility of using an ensemble Kalman filter (EnKF) to retrieve the wind and temperature fields in an isolated convective storm has been tested by applying the technique to observations of the 17 May 1981 Arcadia, Oklahoma, tornadic supercell. Radial-velocity and reflectivity observations from a single radar were assimilated into a nonhydrostatic, anelastic numerical model initialized with an idealized (horizontally homogeneous) base state. The assimilation results were compared to observations from another Doppler radar, the results of dual-Doppler wind syntheses, and in situ measurements from an instrumented tower. Observation errors make it more difficult to assess EnKF performance than in previous storm-scale EnKF experiments that employed synthetic observations and a perfect model; nevertheless, the comparisons in this case indicate that the locations of the main updraft and mesocyclone in the Arcadia storm were determined rather accurately, especially at midlevels. The magnitudes of vertical velocity and vertical vorticity in these features are similar to those in the dual-Doppler analyses, except that the low-level updraft is stronger in the EnKF analyses than in the dual-Doppler analyses.

Several assimilation-scheme parameters are adjustable, including the method of initializing the ensemble, the inflation factor applied to perturbations, the magnitude of the assumed observation-error variance, and the degree of localization of the filter. In the Arcadia storm experiments, in which observations of a mature storm were assimilated over a relatively short (47 min) period, the results depended most on the ensemble-initialization method.

In the data assimilation experiments, too much northerly storm-relative outflow along the south side of the low-level cold pool eventually developed during the assimilation period. Assimilation of Doppler observations did little to correct temperature errors near the surface in the cold pool. Both observational limitations (poor spatial resolution in the radar data near the ground) and model errors (coarse resolution and uncertainties in the parameterizations of moist processes) probably contributed to poor low-level temperature analyses in these experiments.

1. Introduction

Determining the three-dimensional (3D) wind and thermodynamic fields within convective storms is an essential task in storm-scale analysis and will be an important element of storm-scale numerical forecasting. Since the only source of volumetric information on

storm scales¹ in the current operational observing system is the Doppler radar network, much research has been focused on retrieving wind and temperature from radar measurements of Doppler velocity and reflectivity. Over the past 30 years, increasingly sophisticated methods have been developed to deduce the atmospheric state on storm scales from radar observations. Wind retrievals based on multiple-Doppler observations and a continuity constraint (e.g., Armijo 1969; Ray et al. 1980;

* The National Center for Atmospheric Research is sponsored by the National Science Foundation.

Corresponding author address: David C. Dowell, CIMMS, 1313 Halley Circle, Norman, OK 73069.
E-mail: David.Dowell@noaa.gov

¹ The gross structure of a convective storm can be depicted by observations every ~1 km in each coordinate direction. Observations every ~100 m are required to resolve subupdraft-scale features (Carbone et al. 1985).

Scialom and Lemaitre 1990) are particularly feasible because there is a simple geometric relationship between the observations (Doppler velocity) and the retrieved field (the 3D velocity vector). By employing additional constraints, one can in some cases retrieve the 3D wind field from single-Doppler observations (e.g., Laroche and Zawadzki 1994; Xu et al. 1994; Shapiro et al. 1995), but the retrievals tend to be less accurate than multiple-Doppler syntheses.

To diagnose storm processes or initialize forecast models, one must also retrieve the temperature field. For example, convective initiation (Droegemeier and Wilhelmson 1985; Crook 1996), low-level mesocyclogenesis in supercells (Rotunno and Klemp 1985), and the development of long-lived convective systems (Thorpe et al. 1982; Rotunno et al. 1988) are all sensitive to the characteristics of the temperature field near the surface. Since radar does not measure temperature and in situ temperature measurements are available only at isolated locations, determining the temperature field is difficult.

Gal-Chen (1978), Hane et al. (1981), and Brandes (1984) developed methods that retrieve temperature through the equations of motion. The first retrieval step is to determine the 3D velocity field and its time derivative from the Doppler observations. Then, one obtains solutions for pressure and temperature, the unknown variables in the equations of motion. Roux (1985) proposed using an additional constraint—the thermodynamic equation—in order to obtain more accurate temperature and pressure analyses. For all methods, the retrieved temperature is particularly sensitive to the estimate of the time derivative of vertical velocity, which is difficult to determine accurately from Doppler observations owing to errors in the observations, quasi-horizontal scanning, and relatively long periods between consecutive volume scans (Gal-Chen and Kropfli 1984; Crook 1994). Nevertheless, these “traditional” retrievals applied to dual-Doppler observations can identify some features in the temperature field, such as warm anomalies in updrafts at midlevels (Brandes 1984; Hane and Ray 1985).

Rutledge and Hobbs (1983) and Ziegler (1985) proposed using a numerical cloud model as part of thermodynamic and microphysical retrieval. More recently, full assimilation of radar data into numerical models has been proposed as a method of determining the atmospheric state on convective scales (Lilly 1990; Sun et al. 1991; Kapitza 1991; Sun and Crook 1997, 1998). Although data assimilation is often employed as a method for initializing a forecast model, the focus of this paper is on the retrieved atmospheric state during the assimilation period, rather than on a forecast after the assimilation cycle. Unlike the traditional methods (Gal-Chen 1978; Hane et al. 1981; Brandes 1984; Roux 1985) in which the wind field is synthesized and then the temperature field is retrieved, data assimilation methods seek to retrieve all fields simultaneously. Data assimilation

provides a framework in which observation errors can be addressed systematically, and thus the results of data assimilation tend to be less sensitive to random observation errors than traditional methods.

Sun and Crook (1997, 1998) developed a four-dimensional variational data assimilation (4DVAR) system for assimilating radar data into a nonhydrostatic, anelastic numerical cloud model. The 4DVAR method attempts to find the best representation in the model of the observed cloud system by minimizing a cost function, which defines the mismatch between the simulation and the observations. Iterative forward integration of the dynamic model and backward integration of the adjoint model are used to find initial conditions that are associated with a minimum in the cost function. Sun and Crook (1998) applied their technique to Doppler velocity and reflectivity observations of a convective cell in Florida. The vertical velocity, temperature, and humidity fields that were retrieved in both experiments were quite consistent with in situ measurements collected during aircraft penetrations of the convective cell. The 4DVAR system for storm-scale data assimilation has been tested recently, with some success, on other cases (Wu et al. 2000; Sun et al. 2001; Crook and Dowell 2003).

The ensemble Kalman filter (EnKF) (Evensen 1994; Houtekamer and Mitchell 1998) has been proposed as an alternative data assimilation strategy. The EnKF is based on a general theory for determining the most likely state estimate from a background state estimate (i.e., a forecast) and a set of observations (Kalman 1960). Key elements of Kalman filter methods are the spatial and multivariate covariances of the forecast errors. Tests on a variety of problems have indicated that it is practical to estimate these covariances by computing relationships between perturbations in an ensemble of forecasts containing $O[100]$ members (Evensen 1994; Houtekamer and Mitchell 1998; Hamill et al. 2001; Mitchell et al. 2002; Snyder and Zhang 2003, hereafter SZ2003). The EnKF is a sequential assimilation method, which refines the atmospheric state estimate by processing observations during a forward integration of an ensemble of model states. There are two major advantages of an EnKF method over a 4DVAR method. First, it is not necessary to derive and code an adjoint model; thus, the EnKF method is relatively easy to implement once a forecast model has been developed. Second, the forward integration of the forecast ensemble, which in the experiments here is responsible for most of the total computing time, can be executed efficiently on parallel processors. When observations are available only over a limited time period, as in the current experiments, a limitation of the EnKF method is the difficulty of populating the initial ensemble prior to assimilating any observations.

SZ2003, Zhang et al. (2004), and Caya et al. (2004, manuscript submitted to *Mon. Wea. Rev.*, hereafter CSS) tested the EnKF as a method for obtaining convective-

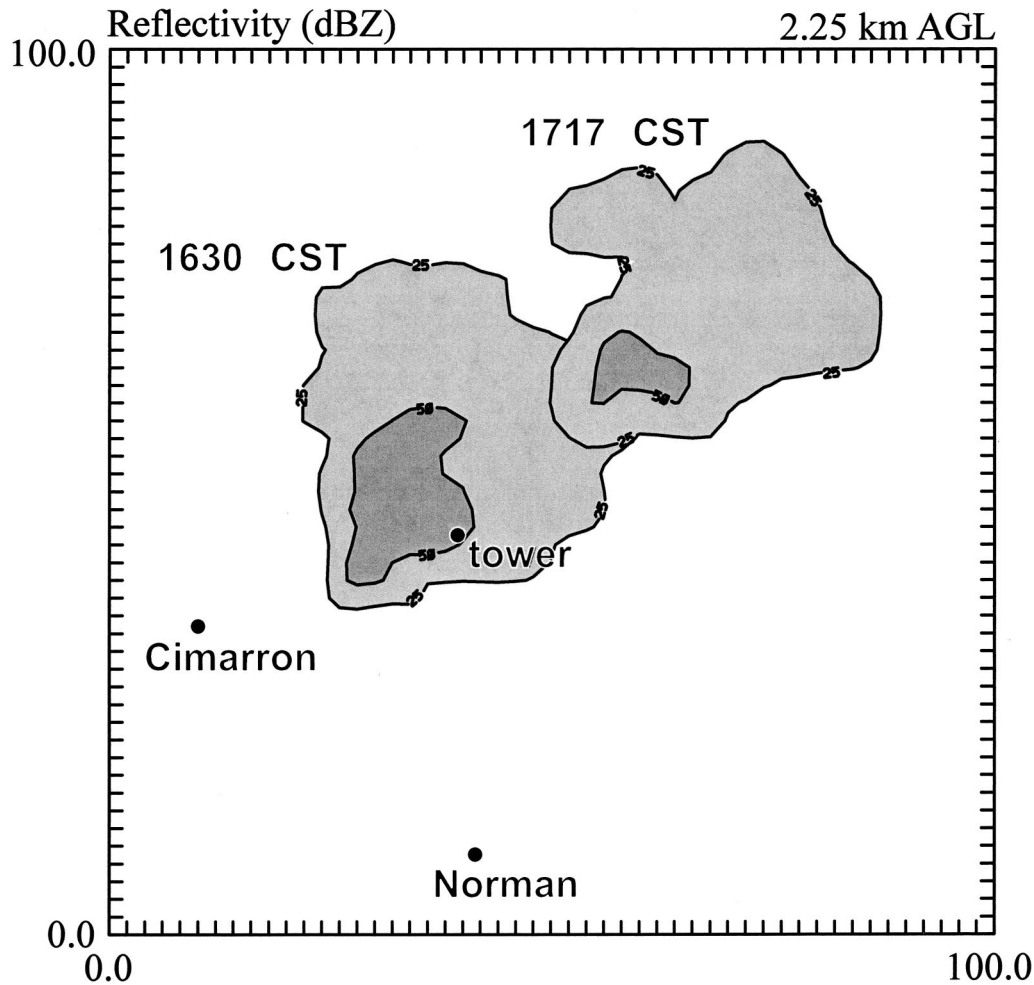


FIG. 1. Map of the locations of the Norman and Cimarron Doppler radars, the instrumented tower, and the Arcadia storm. The reflectivity factor from the Cimarron radar at 2.25 km AGL at 1630 and 1717 CST 17 May 1981 is contoured and shaded at 25 and 50 dBZ. The horizontal dimensions (100 km in each direction) of the region shown correspond to those of the model grid used for the assimilation experiments.

scale state estimates in deep, moist convection from Doppler observations. SZ2003 used the Sun and Crook (1997, 1998) forecast model to simulate an isolated supercell storm in a homogeneous base state. Synthetic radial-velocity observations were produced by sampling the model winds every 5 min relative to the “radar” location. Random errors were added to the synthetic radial-velocity observations, which were produced only at grid points with rainwater. Then, SZ2003 assimilated the synthetic observations back into the forecast model and examined how well the original model fields could be reproduced from the limited sets of observations. The EnKF analyses of the developing supercell closely resembled the model states in the control simulation after assimilation of only a few volumes of synthetic radar data. The covariances between radial velocity and unobserved thermodynamic fields, which were derived

from an ensemble of 50 members, were necessary for producing accurate, efficient retrievals.

We report here on the application of the EnKF to observations of a real thunderstorm. Specifically, we selected the 17 May 1981 Arcadia, Oklahoma, tornadic supercell thunderstorm (Dowell and Bluestein 1997, hereafter DB1997) for detailed study (Fig. 1). Observations of the mature Arcadia storm were collected from two 10-cm research Doppler radars (the “Norman” and “Cimarron” radars) approximately every 5 min for 1 h. The storm also passed over and was sampled by a 444-m-tall instrumented tower. DB1997 discussed the processes of tornadogenesis and tornado dissipation in the Arcadia storm as revealed by dual-Doppler analyses. Weygandt et al. (2002a,b) used the same case for their single-Doppler retrieval and prediction experiments. A 4DVAR study of the Arcadia storm is in progress (Crook

and Dowell 2003) and will be described in more detail in a later paper.

Since operational weather radars are widely separated, individual storms are typically documented well by only one radar at a particular time. To provide examples of retrievals that could be obtained from operational data, we thus assimilated observations from a single radar (in this case the Cimarron radar) into the Sun and Crook (1997, 1998) model in our experiments. We compared the retrieved fields to the following observations: the Norman radar measurements, the results of dual-Doppler wind syntheses, and the instrumented-tower measurements. Although the assimilation procedure estimates all model fields, the focus of this study is specifically the retrieved wind and temperature fields. In section 2, we describe the observations, numerical model, data assimilation system, and diagnostics. In the next section, we describe the 3D wind fields retrieved from single-Doppler observations. In section 4, we focus on the retrieved temperature field at low levels. We close with a summary of results and suggestions for future work.

2. Description of the observations and the data assimilation system

a. Storm environment

The tornado outbreak in Oklahoma on 17 May 1981 occurred within a classic Great Plains severe weather setting (DB1997). The storm of interest, which produced an F2 tornado near Arcadia, from approximately 1700 to 1710 central standard time (CST), formed along a dryline in west-central Oklahoma just before 1500 CST. The observations of the Arcadia storm and its environment that are described in this paper were collected as part of a spring field program organized by the National Severe Storms Laboratory in Norman, Oklahoma (Taylor 1982). Of particular interest here are the Doppler radar data (described in the next subsection) and the environmental soundings.

The storm environment was sampled by rawinsondes every 1–3 h from three different locations in central Oklahoma. Despite the availability of many soundings, no individual sounding appears to represent the environment just southeast of the storm during the period of interest (1630 to 1730 CST). Considerable evolution in the environment was occurring during the afternoon as a short-wave trough at midlevels passed over Oklahoma (DB1997). The base-state sounding in our assimilation experiments (Fig. 2) is a modified version of the sounding at 1430 CST from Edmond, Oklahoma, which is 10 km west of Arcadia (Fig. 2 of DB1997). The following changes we made to the 1430 CST Edmond sounding are consistent with trends observed at all sounding sites between 1400 and 1730 CST as the short-wave trough passed: weakening the stable layer near 700 mb and straightening the hodograph between

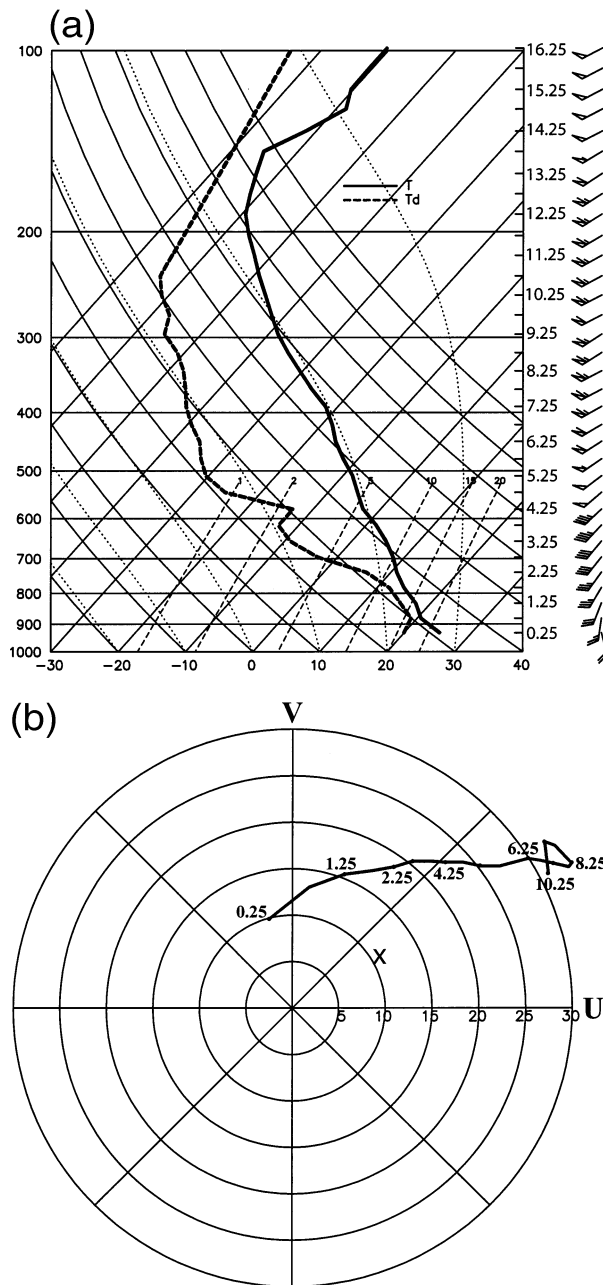


FIG. 2. Environmental conditions in the assimilation experiments. In (a) the skew T -log p diagram, wind barbs (flags) represent 5 m s^{-1} (25 m s^{-1}), temperatures (T) and dewpoints (T_d) (bottom scale) are in $^{\circ}\text{C}$, pressures (left scale) are in mb, and heights (right scale) are in km AGL. (b) Heights are also indicated on the hodograph. The rings are at 5 m s^{-1} intervals. The "X" on the hodograph indicates the mean motion of the Arcadia storm ($U = 9 \text{ m s}^{-1}$; $V = 6 \text{ m s}^{-1}$).

1 and 6 km AGL. In addition, we increased the humidity in the boundary layer; this change was motivated by observations from the instrumented tower in the environment of the storm (DB1997). All of these modifications to the original sounding make the modified base

state more consistent with the base state in the numerical prediction experiments of Weygandt et al. (2002b). The following bulk parameters for the modified sounding (Fig. 2) are conducive to the formation of supercell thunderstorms (Weisman and Klemp 1984): convective available potential energy (computation based on virtual temperature, without condensate loading) of 3400 J kg^{-1} and vertical shear of the horizontal wind of approximately 0.005 s^{-1} in the lowest 6 km AGL.

b. Radar data

The Norman and Cimarron radars (Fig. 1) collected coordinated dual-Doppler volume scans of the mature Arcadia storm that were centered on the following times: 1630, 1634, 1638, 1643, 1647, 1651, 1704, 1710, 1713, and 1717 CST. Additional data were collected later and also much earlier, but these data are not used in the current study. Since the radar scanning was briefly concentrated on another tornadic storm, there is a relatively long interval between the 1651 and 1704 CST volumes. Each volume scan took 3–5 min to complete and consisted of sweeps at 12–15 different elevation angles covering the depth of the storm. The lowest sweeps were at approximately 0.5° elevation angle (300 to 800 m AGL at the range to the main updraft between 1630 and 1717 CST). The next two higher sweeps were at elevation-angle increments of approximately 0.5° , and the remaining sweeps were at 2° – 3° increments. As the storm moved northeastward, the range from the Cimarron (Norman) radar to the updraft and mesocyclone increased from approximately 25 km (35 km) to 55 km (55 km) during the period of interest. The azimuth angles of the Norman and Cimarron observations differed by more than 45° in the updraft region throughout the period.

The radar data that are assimilated and used for verification in this study have been edited by removing noisy/erroneous data and unfolding aliased radial velocities. Data outside the precipitation region (i.e., in “clear air”) were noisy and were removed. In addition, observations in the lowest few sweeps by the Norman radar in the precipitation region beneath the downshear anvil were contaminated by range folding and were deleted (DB1997). We chose to assimilate objectively analyzed velocity and reflectivity observations rather than edited raw observations. Although we could have assimilated raw observations instead, our choice makes the horizontal spacing between adjacent observations the same as the model’s horizontal grid spacing, as in SZ2003’s experiments.

Particularly in vertically sheared flows such as supercell environments, a standard objective analysis of an entire volume to a Cartesian grid (e.g., DB1997) can introduce bias errors in the objectively analyzed data where raw observations are distributed irregularly about a grid point (e.g., near the edge of a data-coverage region). Instead, we applied an objective analysis to each

sweep separately (Sun and Crook 2001), thereby preserving the conical distribution of the data and reducing the potential for vertical interpolation/extrapolation errors. Our objective-analysis method could be described as semi-Cartesian because the x and y coordinates of the objectively analyzed data coincide with those of the scalar grid points in the assimilation model (section 2c). However, the z coordinates do not necessarily coincide with model grid levels; instead, z is the actual height of the observation on the conical scan surface at the particular (x, y) location. We used a Cressman (1959) scheme with a spherical influence region of radius 1000 m to compute interpolated values of the observations at the grid points, which are 2000 m apart in the horizontal. After the objective analysis, the volumes contained 3000–6000 total observations of each type (radial velocity and reflectivity), which were distributed among 12–15 elevation angles.

To simplify the assimilation of observations and the verification of results, we assumed all observations in each volume were collected instantaneously at the central time of the volume. Analyzing the raw observations in a storm-relative reference frame (Gal-Chen 1982) helped to minimize errors associated with this assumption. We computed the radial air motion by subtracting the component of precipitation fall velocity from the objectively analyzed velocity. We employed the following empirical relationship during this procedure: $w_r = -2.6(\rho_0/\rho)^{0.4}Z^{0.107}$, where w_r is the fall velocity (m s^{-1}), ρ is the air density (kg m^{-3}) in the environmental sounding, ρ_0 is the mean air density at sea level, and Z is the reflectivity ($\text{mm}^6 \text{ m}^{-3}$) (Foote and duToit 1969; Joss and Waldvogel 1970).

The Arcadia storm produced golfball-sized hail (DB1997), and this hail was apparently associated with high reflectivity-factor values, some exceeding 65 dBZ. Since the precipitation microphysical scheme in the assimilation model does not include hail, we truncated the reflectivity observations (Weygandt et al. 2002b) at 55 dBZ so that assimilation of reflectivity would yield only physically plausible magnitudes of rainwater.

c. Numerical cloud model and control data assimilation experiment

The forecast model employed in the data assimilation experiments is the same nonhydrostatic, anelastic numerical cloud model used by Sun and Crook (1997, 1998) for their 4DVAR experiments and by SZ2003 for their idealized EnKF experiments. The prognostic variables are the three Cartesian velocity components u , v , and w ; the perturbation liquid-water potential temperature θ'_l ; the rainwater mixing ratio q_r ; and the total-water mixing ratio q_t . Pressure, cloud water, and water vapor are diagnosed from the predicted quantities. The warm-rain microphysical scheme in the model (Sun and Crook 1997) includes the processes of condensation, autoconversion of cloud water to rainwater, accretion of

cloud water by rainwater, and evaporation of rainwater and cloud water. The base-state model fields are preserved at lateral boundaries where there is inflow, and the model fields at lateral boundaries where there is outflow are computed by linear extrapolation (Sun and Crook 1994).

The model domain is 100 km wide in each horizontal direction (Fig. 1) and 17 km tall. In most of the assimilation experiments, the horizontal grid spacing was 2 km. Although this grid spacing makes the computation feasible on our single-processor computer, the grid is suitable for resolving only the gross features of the Arcadia storm. The results of a higher-resolution experiment employing a 1-km horizontal grid spacing are described in section 3c. The vertical grid spacing was 500 m in all experiments.

We produced an ensemble of 50 initial model states by adding random perturbations to a first-guess state. The first-guess model fields were horizontally homogeneous with vertical profiles identical to those in the estimated environmental sounding (Fig. 2). No attempt was made to model inhomogeneities in the storm environment (i.e., surrounding soundings and other environmental data were not assimilated), other than those introduced by the radar data. This simplification is consistent with our emphasis on wind and temperature retrievals within the domain of radar-data coverage. Assimilation of both radar data and environmental data could be a subject of future experiments in which the emphasis is more on forecasts than on retrievals.

Initializing an ensemble for storm-scale data assimilation is not straightforward (SZ2003; Zhang et al. 2004), and our initialization method is not necessarily optimal. Our “control assimilation experiment” described below had the best verification scores among a set of experiments; sensitivities of the results to some assimilation-scheme parameters are discussed in section 3b. For simplicity, SZ2003 created individual ensemble members by adding random noise to the environmental state. We improved the results of our experiments (section 3b) by adding more coherent perturbations. To initialize an ensemble member, we added 40 ellipsoidal perturbations to each model field in random locations over a limited (40 km wide and 12 km tall) portion of the domain that was centered approximately on the observed updraft location at the time of the first volume of radar data. Centering the perturbation region on the observed storm can help the assimilation (SZ2003). This initialization method is particularly feasible in research experiments but is also possible in a forecast situation; one could wait for first storm echoes to appear on radar and then initialize an ensemble at a prior time. The magnitudes at the centers of the perturbations were 5 m s⁻¹, 5 m s⁻¹, 5 K, 5 g kg⁻¹, and 5 g kg⁻¹ for u , v , θ'_i , q_r , and q_i , respectively, and the magnitudes decreased to zero at a horizontal (vertical) radius of 10 km (2.5 km). Each perturbation was random in sign, and perturbations were additive in locations where they

overlapped. A correction procedure applied after the perturbation step eliminated negative mixing ratios. Since significant vertical-velocity perturbations developed in the model in response to the other perturbations, we did not add any perturbations to the initial w fields. Before assimilating the first data volume, we integrated the ensemble members for 20 min. During this initial forecast period, incipient supercells (convective cells with midlevel rotation) developed in the ensemble of model states (Fig. 3a). Many of these incipient cells were spurious in that they were not collocated with the observed storm. As in the experiments of SZ2003, some of the spurious cells that were outside the domain of Doppler observations survived throughout the assimilation (e.g., Fig. 3b). Yet, these spurious cells were hardly noticeable in the ensemble mean (Fig. 3c) because they were isolated and rather randomly distributed. In more recent assimilation experiments with other cases (not shown), we have noticed that assimilating reflectivity observations everywhere, which was not implemented in the experiments described below, greatly suppresses spurious cells.

We assimilated observations from one radar only—the Cimarron radar—into the model in all experiments. We chose the Cimarron data, as did Weygandt et al. (2002a), because the storm was closer to the Cimarron radar than the Norman radar at the beginning of the assimilation period, and there was no noticeable contamination by range folding in the Cimarron data. Our EnKF method of assimilating objectively analyzed observations into the numerical model was similar to that employed by SZ2003. Like Snyder and Zhang, we processed the observations serially (one at a time) by assuming that the observation errors were uncorrelated in space and time. Although we did not verify that errors in the raw observations were indeed uncorrelated, we did choose an objective-analysis method (section 2b) that does not introduce any additional correlation; that is, separate objectively analyzed observations are computed from mutually exclusive sets of raw observations. We used the following equations to update the model-state estimates during the assimilation of each observation:

$$\bar{x}^a = \bar{x}^f + WK[y^o - \overline{H(\mathbf{x}^f)}], \quad (1)$$

$$x_n^a = \bar{x}^a + (x_n^f - \bar{x}^f) + WK\beta[\overline{H(\mathbf{x}^f)} - H(\mathbf{x}_n^f)], \quad (2)$$

where n is an index that identifies a particular ensemble member, an overbar indicates an ensemble mean, x_n^f is a forecast value of a model field, x_n^a is an analysis value of a model field, \mathbf{x} is a vector representation of the entire model state, y^o is an observation, H is an operator that maps a model forecast to the observation type and location, and W is a weight that depends on the distance from the observation to the model grid point where x is located. The Kalman gain K and the β factor in (1) and (2) are computed as follows:

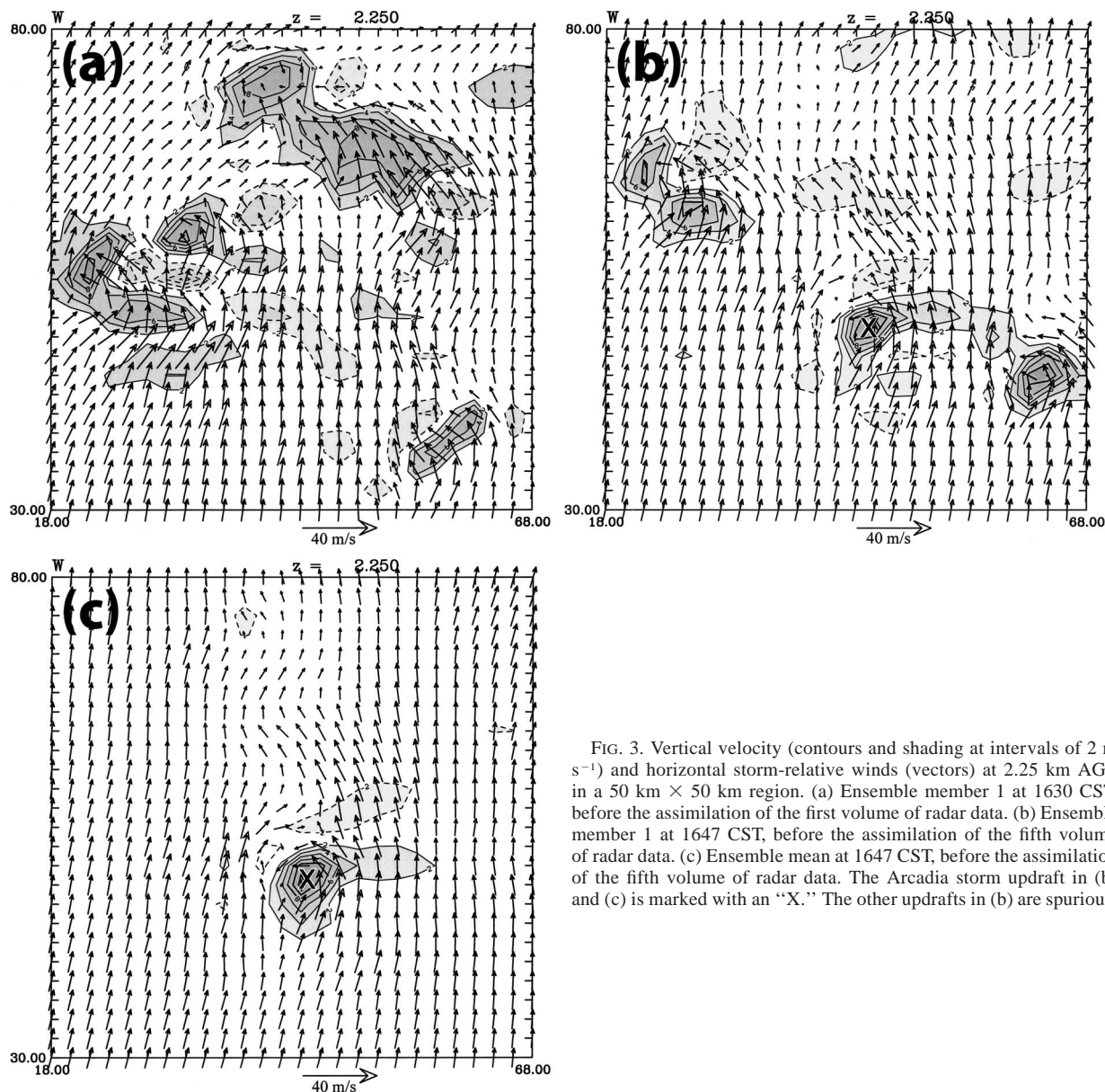


FIG. 3. Vertical velocity (contours and shading at intervals of 2 m s^{-1}) and horizontal storm-relative winds (vectors) at 2.25 km AGL in a $50 \text{ km} \times 50 \text{ km}$ region. (a) Ensemble member 1 at 1630 CST, before the assimilation of the first volume of radar data. (b) Ensemble member 1 at 1647 CST, before the assimilation of the fifth volume of radar data. (c) Ensemble mean at 1647 CST, before the assimilation of the fifth volume of radar data. The Arcadia storm updraft in (b) and (c) is marked with an "X." The other updrafts in (b) are spurious.

$$K = \frac{\frac{1}{N-1} \sum_{n=1}^N (x_n^f - \bar{x}^f)[H(\mathbf{x}_n^f) - \overline{H(\mathbf{x}^f)}]}{\sigma^2 + \frac{1}{N-1} \sum_{n=1}^N [H(\mathbf{x}_n^f) - \overline{H(\mathbf{x}^f)}]^2}, \quad (3)$$

$$\beta = \left\{ 1 + \frac{\sigma^2}{\sigma^2 + \frac{1}{N-1} \sum_{n=1}^N [H(\mathbf{x}_n^f) - \overline{H(\mathbf{x}^f)}]^2} \right\}^{-1}, \quad (4)$$

where N is the number of ensemble members, and σ^2 is the specified observation-error variance. The β factor arises because the scheme does not use perturbed observations (Whitaker and Hamill 2002). At large dis-

tances from an observation, the covariance estimate in (3) tends to be small and to contain considerable sampling error owing to the limited ensemble size. To reduce the influence of such errors on the analysis, we allow an observation to update only state variables at nearby grid points (Houtekamer and Mitchell 2001). Specifically, we multiply the Kalman gain by a weight W that decreases smoothly from 1 at the observation location to 0 at the edge of a spherical influence region of radius 6 km. The functional form of W is taken from the compactly supported fifth-order correlation function in Eq. (4.10) of Gaspari and Cohn (1999). Our results are relatively insensitive to modest variations in the length scale of the weighting function (section 3b), as were SZ2003's results. Nevertheless, there still might be some

potential for improving EnKF performance by developing a diagnostic procedure for choosing the optimal weighting function, which could be anisotropic and/or flow dependent.

The assimilation algorithm processes one observation at a time. The first step during the assimilation of an observation y^o is to apply the observation operator H to each forecast state \mathbf{x}_n^f . Then, the inner loops of the algorithm apply the following procedure to each model field at each grid point within the neighborhood of the observation: calculate (3) and (4), update the ensemble mean with (1), and then update the ensemble members with (2). If an additional observation at the same time is available, then the updated (analysis) state estimates \mathbf{x}^a become the new prior estimates \mathbf{x}^f . After the assimilation algorithm is applied to all observations at the current time, the ensemble of forecasts is advanced to the next time when observations are available.

We assimilated both radial-velocity and reflectivity-factor observations in our experiments. All prognostic model fields (u , v , w , θ'_i , q_r , and q_i) were updated when the filter was applied to radial velocity. We assimilated reflectivity observations only at locations with valid radial-velocity data and only updated the q_r field when assimilating reflectivity observations; since q_r , q_i , and θ'_i are interdependent variables in the model (Sun and Crook 1997), we adjusted θ'_i and q_i accordingly to account for changes in q_r produced by the filter. Initial attempts to update all model fields when processing reflectivity observations did not improve the overall results; more research is needed to determine the best way to assimilate reflectivity (CSS). Simply using the reflectivity observations to update q_r in the current experiments helped maintain a realistic structure of the precipitation core and improved the velocity-verification scores relative to those in experiments in which we did not assimilate reflectivity.

Owing to both the conical distribution of the objectively analyzed observations and the grid staggering in the model, observation locations do not coincide with grid points in the model. We used trilinear interpolation to evaluate the model fields at observation locations. During the assimilation of radial-velocity observations, we determined $H(\mathbf{x}_n^f)$ by computing the component of the trilinearly interpolated velocity in the direction of the radar beam. To determine the reflectivity values in the model, we assumed the rainwater had a Marshall–Palmer drop-size distribution with $n_0 = 8 \times 10^6 \text{ m}^{-4}$ (Sun and Crook 1998). This assumption leads to the following relationship between reflectivity and rainwater mixing ratio: $Z = 2.04 \times 10^4 \text{ mm}^6 \text{ m}^{-3} (\rho q_r)^{1.75}$, where ρ is the air density (kg m^{-3}), and q_r is (g kg^{-1}).

It is difficult to quantify the magnitude of the observation-error variance in (3) and (4). Errors in estimates of mean radial velocity owing to inhomogeneities of velocity and reflectivity within the sampling volume are believed to have a standard deviation of $\sim 1 \text{ m s}^{-1}$ (Doviak et al. 1976). Significantly larger errors might be

produced by range folding, sidelobes, uncertainty in beam position, uncertainty in the relationship between reflectivity and terminal fall velocity, and inaccuracy in the steady-state assumption over the period required to obtain a data volume. Xu et al. (2003) estimated that the standard deviation of Doppler-velocity errors was 2.4 m s^{-1} in their case study, but the applicability of their study to the current one is limited because the radar characteristics are different and their observations were of relatively calm weather. Objective analysis tends to reduce the magnitude of error, but not necessarily at grid points where the surrounding raw measurements are irregularly distributed. In our control assimilation experiment, we specified $\sigma_{v_r} = 2 \text{ m s}^{-1}$ for the objectively analyzed radial velocity observations and $\sigma_{\text{dbz}} = 5 \text{ dBZ}$ for the reflectivity-factor observations. Since the verification scores were not worsened significantly by assuming either $\sigma_{v_r} = 3$ or 4 m s^{-1} (section 3b), we would not rule out the possibility that actual error standard deviations are this great. Lacking a more rigorous alternative, we assumed the observation-error variances were uniform throughout the domain of data coverage.

One other aspect of the data assimilation scheme required some tuning. We found it somewhat helpful to inflate the ensemble occasionally during the assimilation (Anderson and Anderson 1999; Hamill et al. 2001). Inflation counteracts the tendency for ensemble spread to become too small; this tendency is particularly pronounced for the EnKF formulation used here, which systematically underestimates the analysis uncertainty owing to the limited ensemble size (van Leeuwen 1999) and model errors. In the control experiment, we inflated each model variable in each ensemble member by 5% just before assimilating the first observation in each volume, as follows: $x_n^f \leftarrow x_n^f + 0.05(x_n^f - \bar{x}^f)$. In a set of otherwise identical experiments with 0%, 5%, 10%, and 20% inflation, 5% inflation was associated with the lowest rms differences between EnKF and dual-Doppler analyses; applying the other inflation factors increased the rms differences by less than 2%. Other than the inflation, no explicit effort has been made to account for model errors. In future experiments, one might consider parameterizations of model error (Mitchell and Houtekamer 2000; Mitchell et al. 2002).

d. Diagnostics

Before describing the assimilation results (section 3), we provide an overview of the diagnostics used to evaluate the results. Whereas diagnostics in simulated-data experiments (e.g., SZ2003) involve statistical comparisons between the retrieved and true states, the statistics here summarize differences between retrieved and *observed* fields and are thus affected by observation errors. Furthermore, the incompleteness of the observations (i.e., the lack of volumetric observations of most state variables) makes it difficult to evaluate the results.

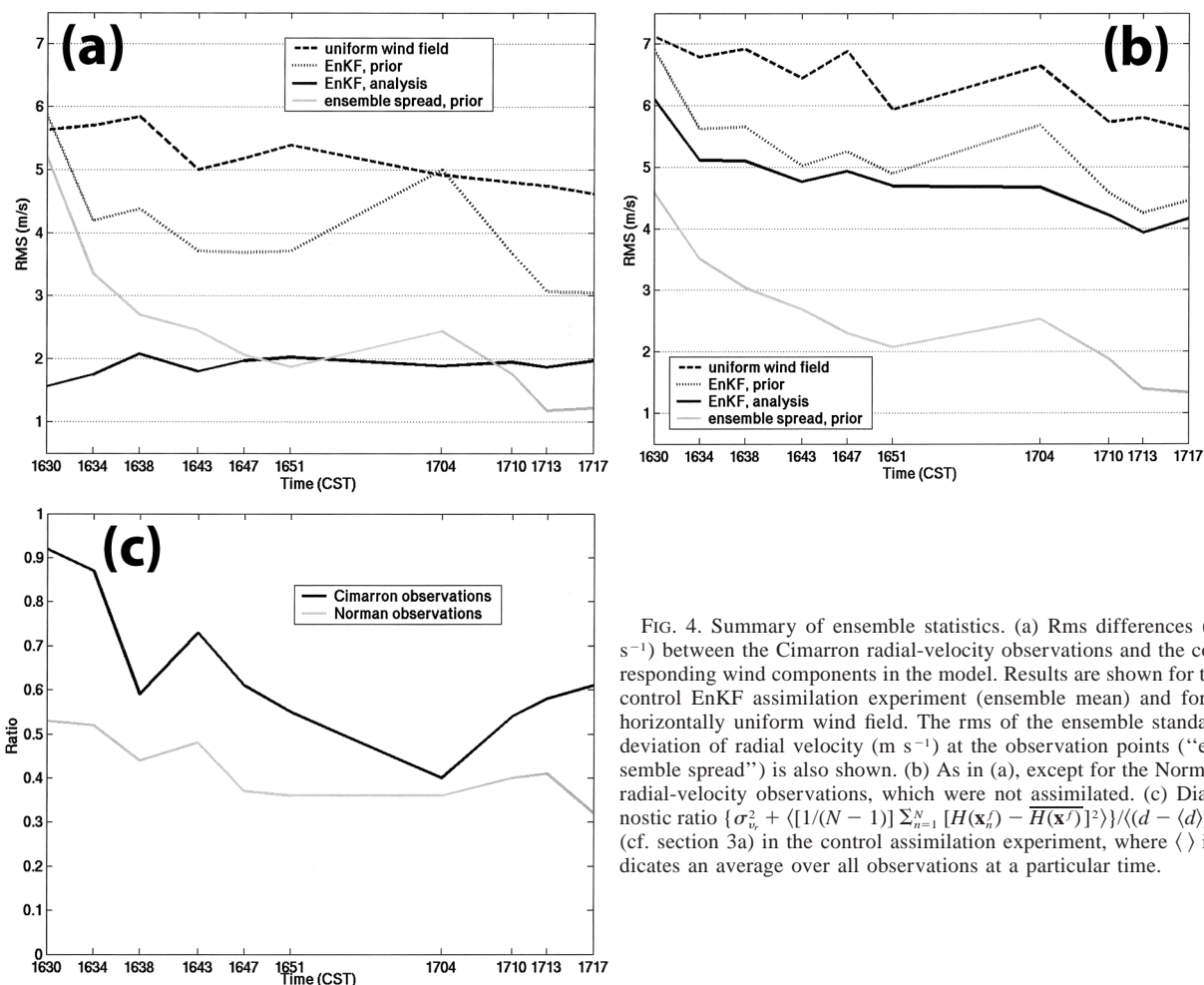


FIG. 4. Summary of ensemble statistics. (a) Rms differences (m s^{-1}) between the Cimarron radial-velocity observations and the corresponding wind components in the model. Results are shown for the control EnKF assimilation experiment (ensemble mean) and for a horizontally uniform wind field. The rms of the ensemble standard deviation of radial velocity (m s^{-1}) at the observation points (“ensemble spread”) is also shown. (b) As in (a), except for the Norman radial-velocity observations, which were not assimilated. (c) Diagnostic ratio $\{\sigma_v^2 + \langle [1/(N-1)] \sum_{i=1}^N [H(\mathbf{x}_i) - \overline{H(\mathbf{x})}]^2 \rangle\} / \langle (d - \langle d \rangle)^2 \rangle$ (cf. section 3a) in the control assimilation experiment, where $\langle \rangle$ indicates an average over all observations at a particular time.

One basic diagnostic described in section 3 is the fit of the EnKF analyses to the independent wind observations from Norman (Fig. 4). The Norman radial-velocity observations, which were objectively analyzed in the same way as the Cimarron observations (section 2b), have errors of at least 2 and possibly as much as 4 m s^{-1} (section 2c). This magnitude of observation error represents a lower bound on the fit.

Some of the other diagnostics in section 3 are based on the differences between EnKF analyses and dual-Doppler wind syntheses. We simplified the dual-Doppler wind syntheses by objectively analyzing the Cimarron and Norman observations on a standard Cartesian grid and using a large enough (2.0 km) Cressman radius of influence to fill the portion of the grid within the precipitation core with objectively analyzed data. [In contrast, we used a smaller radius of influence and did not employ a standard Cartesian grid for the single-Doppler analyses (section 2b).] Other than the larger radius of influence, the dual-Doppler synthesis method was identical to DB1997’s method.

Like Weygandt et al. (2002a), we computed differences between the retrieved winds and the azimuthal

(aka “cross-beam”) horizontal wind components in the dual-Doppler analyses (e.g., Fig. 5). The azimuthal horizontal wind component is $v_a = u \cos a_1 - v \sin a_1$, where a_1 is the azimuth angle from the Cimarron radar. An error analysis (not shown) indicates a lower bound of approximately $1.5 \sigma_{v_r}$ for errors in dual-Doppler estimates of azimuthal components at low and midlevels, where the scans are quasi horizontal; larger errors would be expected at higher elevation angles. (Here, σ_{v_r} refers to the actual error standard deviation rather than the assumed magnitude during the assimilation.) Thus, the comparisons to the dual-Doppler analyses are more subject to random errors than the comparisons to the Norman observations. We restrict the comparisons to the dual-Doppler analyses to those grid points within 60 km of each radar, where the quality of the dual-Doppler syntheses is relatively high because (i) observations extend downward to within 1 km of the surface, (ii) the between-beam angle is greater than 40° , and (iii) the Norman data are minimally contaminated by range folding. The main updraft and mesocyclone of the Arcadia storm were within 60 km of the radars throughout the period of interest.

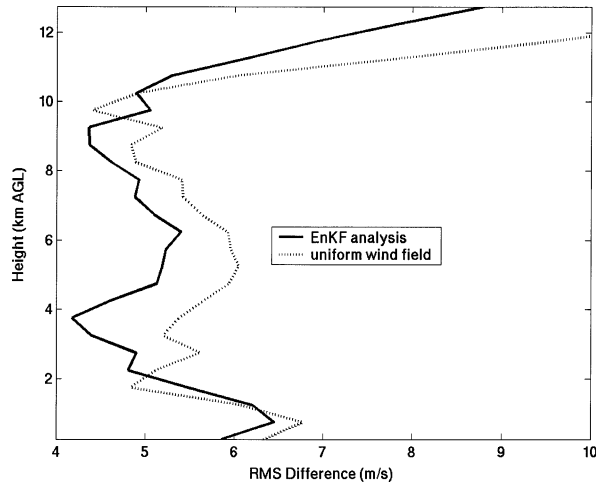


FIG. 5. Rms differences (m s^{-1}) between the azimuthal horizontal wind components (the horizontal components normal to the Cimarron radar beams) in the dual-Doppler analyses and those in the ensemble-mean states of the control EnKF assimilation experiment. Rms differences between the dual-Doppler analyses and the uniform-wind reference state are also indicated. Statistics are averaged over the first four observation times (1630, 1634, 1638, and 1643 CST) and are plotted as a function of height.

The domain-averaged rms measures (e.g., Figs. 4 and 5) are convenient computationally but do not necessarily provide a good estimate of retrieval quality for isolated features such as the main updraft and mesocyclone. Therefore, section 3 also includes quantitative and qualitative comparisons that focus on these features specifically.

SZ2003's synthetic-data experiments were "perfect model" experiments; that is, the environmental sounding and model physics in the assimilation were the same as those in the reference simulation from which the "observations" were generated. In contrast, in the current experiments, model error affects the accuracy of the retrieved fields. The numerical approximation of the dynamical equations, the parameterization of the turbulent mixing, the lack of surface fluxes, and the approximated microphysical processes impact the rms differences between the retrieved and observed winds. For example, recent EnKF experiments with synthetic data (to be described in a later paper) indicate that the cumulative effects over ~ 1 h of errors in a model's precipitation microphysical scheme could add a few meters per second to rms wind errors. Even errors in the base-state wind estimates alone could add a few meters per second to the rms differences between the retrieved and observed winds.

Since both observation and forecast errors are believed to be large for these experiments, it is difficult to determine whether the several-meters-per-second rms differences between the azimuthal winds in the EnKF and dual-Doppler analyses (e.g., Fig. 5) indicate inaccurate dual-Doppler analyses, suboptimal EnKF performance, or both. When comparing different assimilation

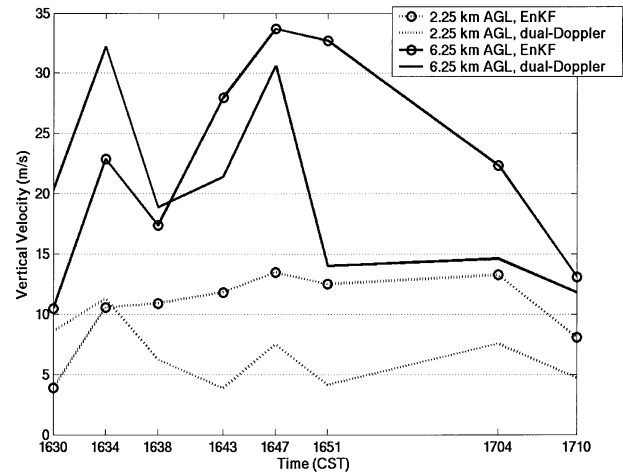


FIG. 6. Maximum vertical velocity (m s^{-1}) in the main storm updraft in the EnKF and dual-Doppler analyses.

experiments, we will nevertheless assume that smaller rms differences indicate more accurate wind retrievals.

3. Single-Doppler wind retrievals

a. Control assimilation experiment

Ten volumes of objectively analyzed Cimarron radar data over a period of 47 min were processed in the control assimilation experiment with the method described in section 2c. The results of the control experiment can be evaluated in multiple ways. First, we analyze differences between the retrieved wind fields and the radial wind observations from the Cimarron radar (the observations that were assimilated; Fig. 4a), the independent wind observations from the Norman radar (Fig. 4b), and the results of dual-Doppler wind syntheses (Fig. 5). Trends in the statistics are somewhat ambiguous because they depend on many factors that change during the assimilation period, including storm structure, storm location, radar scanning strategies, and perhaps assimilation quality. To help interpret the statistics, we therefore provide a basis for relative comparison. A simple reference state that we would hope to improve upon by assimilating observations is one in which the wind at each vertical level is uniform and is specified by the environmental profile (Fig. 2). Statistics corresponding to this "uniform wind" assumption are illustrated by the dashed lines in Figs. 4 and 5.

The difference between an observation and a forecast, commonly called the innovation and represented by d , results from both observation and forecast errors: $d = y^o - \overline{H(\mathbf{x}^f)} = \varepsilon^o - \varepsilon^f$, where observation error is defined as $\varepsilon^o = y^o - H(\mathbf{x}^t)$, forecast error is defined as $\varepsilon^f = \overline{H(\mathbf{x}^f)} - H(\mathbf{x}^t)$, and \mathbf{x}^t is the true state. In our experiments, the rms of d for both the observations that were and were not assimilated generally decreased with time, particularly after the assimilation of the first vol-

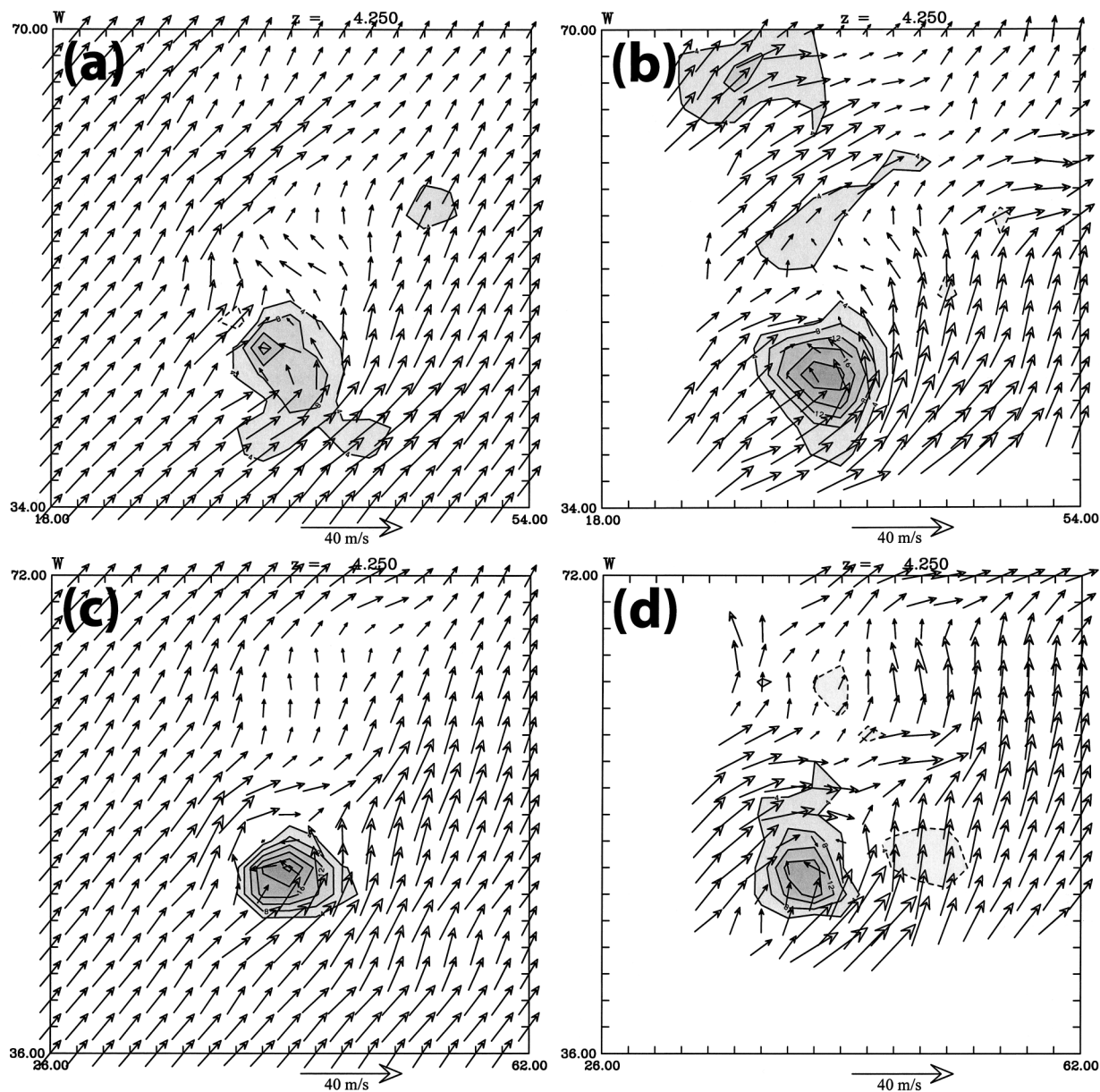


FIG. 7. Vertical velocity (contours and shading at intervals of 4 m s^{-1}) and horizontal storm-relative winds (vectors) at 4.25 km AGL in $36 \text{ km} \times 36 \text{ km}$ regions. (a) Ensemble-mean analysis in the control assimilation experiment at 1634 CST. (b) Dual-Doppler analysis at 1634 CST. (c) Ensemble-mean analysis in the control assimilation experiment at 1704 CST. (d) Dual-Doppler analysis at 1704 CST. (e) Ensemble-mean analysis in the control assimilation experiment at 1704 CST. (f) Dual-Doppler analysis at 1704 CST. The region that is plotted in Fig. 14 is indicated by the dashed box in (e) and (f).

ume of radar data (dotted lines in Figs. 4a and 4b). Furthermore, the verification statistics of the ensemble-mean forecasts tended to be increasingly better than those of the uniform-wind reference state. The exception was at 1704 CST, following a relatively long (13 min) forecast over the period of missing observations.

After each set of Cimarron observations was assimilated, the rms fit to these observations was approximately 2 m s^{-1} (solid line in Fig. 4a); this degree of fit to the observations is consistent with the assumed mag-

nitude of observation-error variance. At each observation time, assimilating the Cimarron observations also decreased the rms differences with respect to the measurements from the Norman radar, which were not assimilated (dotted and solid lines in Fig. 4b).

Another diagnostic tool that we employed was a consistency check. If forecast and observation errors are independent, then

$$\sigma_d^2 = \sigma_o^2 + \sigma_f^2, \quad (5)$$

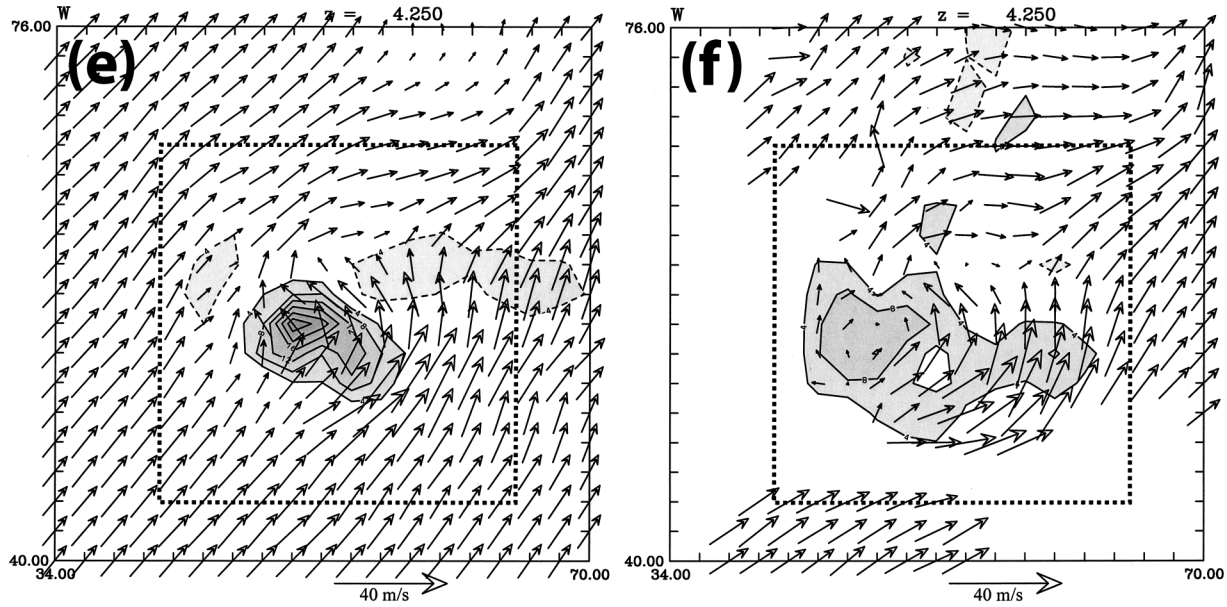


FIG. 7. (Continued)

where σ_d^2 , σ_o^2 , and σ_f^2 are the variances at a particular time and location of the innovation, the observation error, and the forecast error, respectively [see, e.g., Eq. (21) of Dee 1995]. The EnKF assumes that deviations of the ensemble members from the mean are representative of forecast errors, and that σ_f^2 can be estimated from the ensemble. For the radial-velocity observations in our experiments, we assumed $\sigma_o^2 = \sigma_v^2 = (2 \text{ m s}^{-1})^2$. If these assumptions are correct, then the following consistency relation, which is expressed for an average over all observations at a particular time, follows from (5):

$$\frac{\sigma_{v_r}^2 + \left\langle \frac{1}{N-1} \sum_{n=1}^N [H(\mathbf{x}_n^f) - \overline{H(\mathbf{x}^f)}]^2 \right\rangle}{\langle (d - \langle d \rangle)^2 \rangle} \approx 1, \quad (6)$$

where $\langle \rangle$ indicates an average over all observations at a particular time, and the second term in the numerator in (6) is the square of ensemble spread in radial velocity (Figs. 4a and 4b). In the control assimilation experiment, the ratio in (6) for the prior state estimates was in the range 0.40–0.91 for the Cimarron radial-velocity observations, and in the range 0.32–0.53 for the independent Norman observations (Fig. 4c). Consistent with these results, rank histograms (Hamill 2001) tended to have a “U” shape (not shown). According to these diagnostics, our assumed observation-error variance could have been too small on average, thus making the numerator in (6) too small. Another possibility, and one that is a persistent problem in ensemble forecasting and assimilation, is that the ensemble spread was too small. As mentioned previously, however, simply inflating the ensemble more does not improve the verification scores of the ensemble mean. Therefore, more robust methods

for increasing spread in appropriate fields at appropriate locations would be helpful.

To evaluate further the retrieval of unobserved wind information, we compared the horizontal azimuthal wind components (section 2d) in the EnKF analyses to those in the dual-Doppler analyses. A vertical profile of rms differences (Fig. 5) indicates the best agreement between approximately 2 and 10 km AGL. The value of the assimilation relative to the uniform-wind reference state also tends to be greatest in this layer. Above 10 km, the rms differences (Fig. 5) increase quickly with height. This increase could be primarily an indication of large errors in the dual-Doppler analyses (Doviak et al. 1976). At the lowest two levels, one factor that could have contributed to the relatively large rms differences was erroneous downward extrapolation of data during the objective-analysis step of the dual-Doppler wind synthesis. A second factor is the slower development of the mesocyclone at low levels than at midlevels in the assimilation. Both of these factors are discussed in more detail shortly.

We focus now on the retrievals of the updraft and mesocyclone characteristics because these retrievals provide information about the quality of the assimilation that is less apparent in the domain-averaged statistics. Assimilation of the first Cimarron data volume produces positive anomalies in vertical velocity, temperature, and cloud water at the approximate location of the main midlevel updraft in the Arcadia storm (not shown), but the magnitude of the updraft in the EnKF analysis at 1630 CST is only about half of what is indicated by the dual-Doppler analysis (Fig. 6). Assimilation of the next observation volume results in a stronger updraft. After 1634 CST (1638 CST), the strength of the updraft at

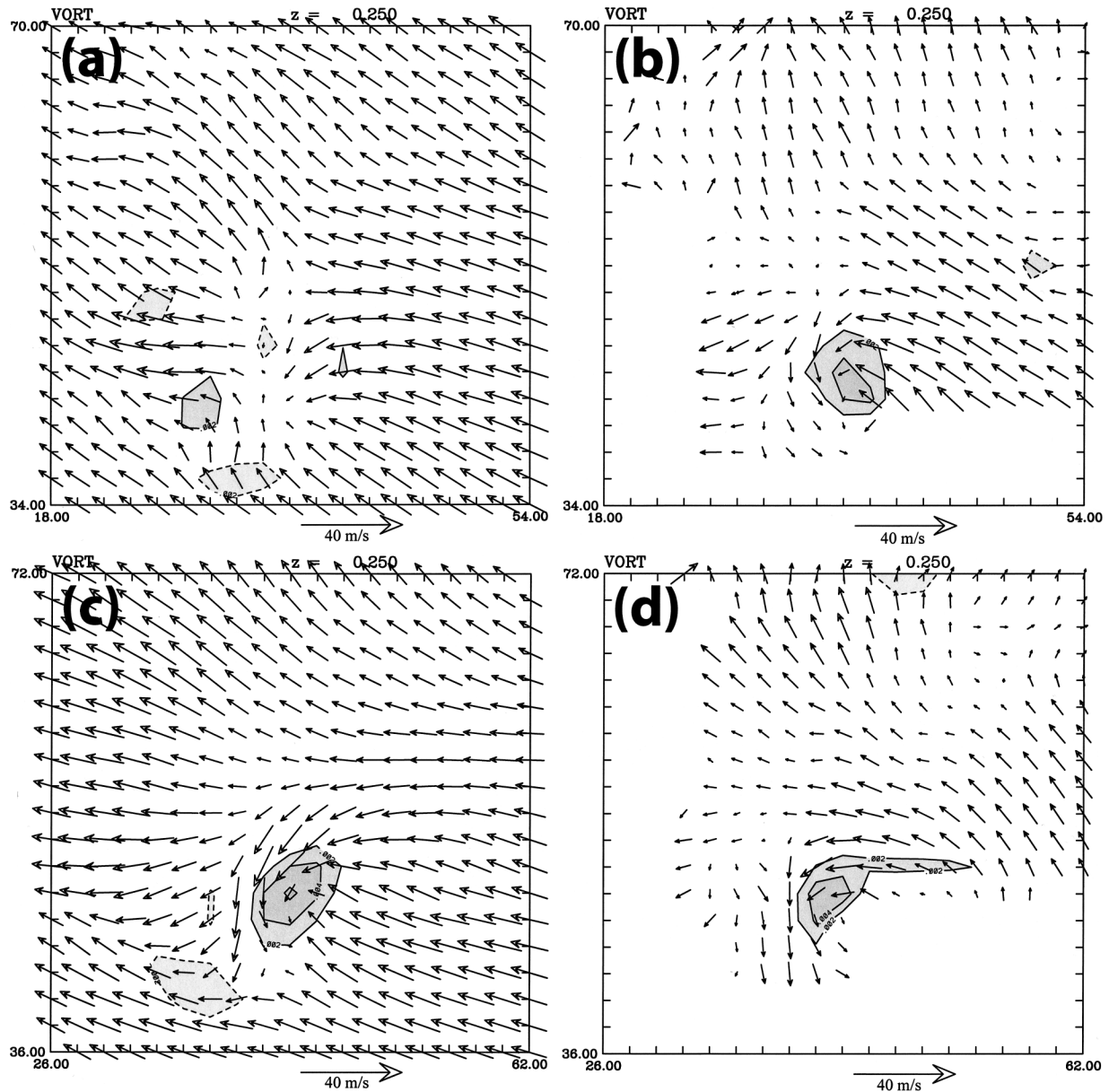


FIG. 8. Vertical vorticity (contours and shading at intervals of 0.002 s^{-1}) and horizontal storm-relative winds (vectors) at 0.25 km AGL in $36 \text{ km} \times 36 \text{ km}$ regions. (a) Ensemble-mean analysis in the control assimilation experiment at 1634 CST. (b) Dual-Doppler analysis at 1634 CST. (c) Ensemble-mean analysis in the control assimilation experiment at 1647 CST. (d) Dual-Doppler analysis at 1647 CST. (e) Ensemble-mean analysis in the control assimilation experiment at 1704 CST. (f) Dual-Doppler analysis at 1704 CST. The region that is plotted in Fig. 14 is indicated by the dashed box in (e) and (f).

2.25 km AGL (6.25 km AGL) exceeds that in the dual-Doppler analysis. The percentage difference is particularly large at the lower level. The radar observations probably did not resolve some of the convergence near the ground (DB1997); therefore, the dual-Doppler analysis underestimates the low-level updraft strength. Both the EnKF and dual-Doppler analyses indicate updraft strengthening at 6.25 km between 1638 and 1647 CST and weakening between 1647 and 1710 CST (Fig. 6).

The locations of the midlevel updraft in the EnKF

assimilation and dual-Doppler analysis are broadly consistent (Fig. 7). In addition, the depictions of the cyclonic flow within the main updraft, the anticyclonic flow along the northwestern flank of the updraft, and the other horizontal wind perturbations to the north of the main updraft are similar. The horizontal wind field is smoother in the assimilation than in the dual-Doppler analysis, probably because the former is only provided single-Doppler observations and is also not constrained to satisfy the observations exactly. One feature that is

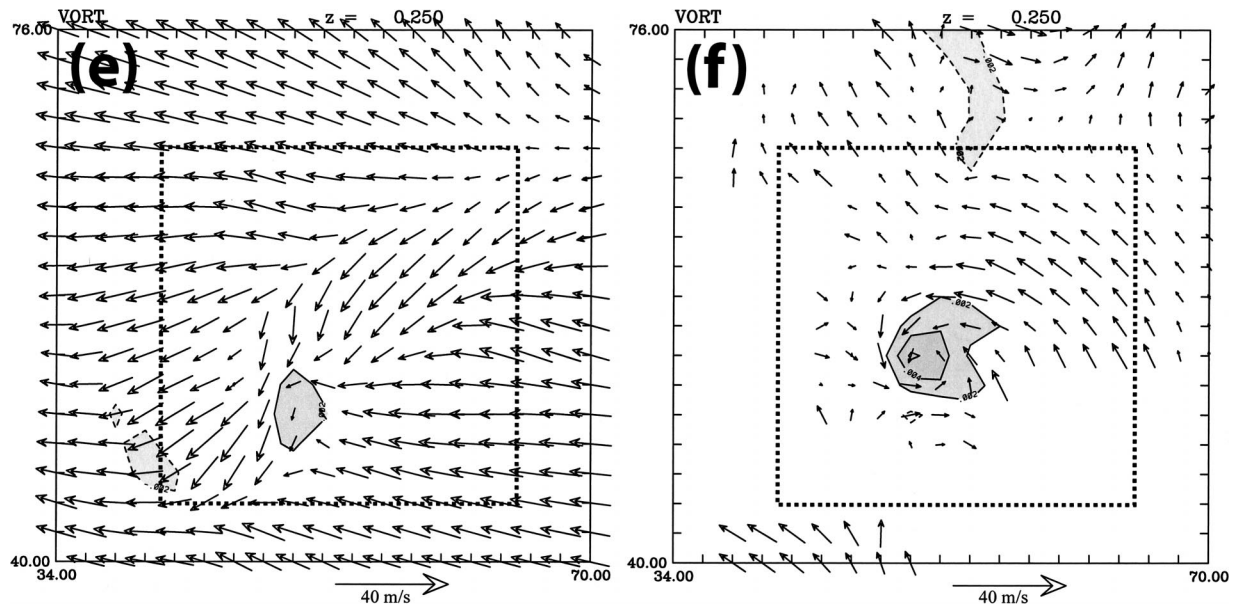


FIG. 8. (Continued)

not well resolved in the EnKF analysis is a weak left-split updraft (DB1997) that is indicated by the dual-Doppler analysis (northwest part of Fig. 7b). This feature was rather short-lived and is not apparent in the dual-Doppler analyses after 1643 CST.

At low levels, the assimilation procedure has more difficulty producing a mesocyclone that is consistent with the dual-Doppler analyses (Fig. 8). Since the lowest Doppler observations in the updraft region (section 2b) are actually a few hundred meters above the level shown in Fig. 8, we are evaluating the model response at the lowest grid level to assimilating observations at higher levels; the dual-Doppler analyses at 250 m AGL that are shown for comparison contain information extrapolated downward from above. After the assimilation of two data volumes, the EnKF analysis indicates only minor vorticity perturbations at the lowest level (Fig. 8a); in contrast, the dual-Doppler analysis indicates a well-developed low-level mesocyclone (Fig. 8b). Some other differences in the retrieved low-level horizontal winds might be explained more by errors in the dual-Doppler analyses. Owing to the aforementioned downward extrapolation, the objective analysis produced data at the lowest grid level from observations at higher actual heights for increasing ranges from the radar. Since the environmental winds veered with height (Fig. 2), the synthesis method would have introduced a tendency for veering winds with increasing range from the radar (i.e., toward the northeast) in the dual-Doppler analyses, as is indicated (Figs. 8b, 8d, and 8f).

After the assimilation of five data volumes, the EnKF analysis does indicate a low-level mesocyclone broadly consistent with the dual-Doppler analysis, in terms of the vorticity magnitude and the strength of the storm-

relative northerly winds on the west side (Figs. 8c and 8d). However, the EnKF and dual-Doppler analyses differ again significantly later in the period. At 1704 CST, during the tornadic stage of the Arcadia storm, the EnKF analysis indicates a low-level mesocyclone that is too weak and too far southwest (Figs. 8e and 8f). We speculate that the failure to maintain a strong low-level mesocyclone in the assimilation results from coarse resolution in the model and errors in the low-level temperature field, as discussed later in sections 3c and 4.

Independent measurements (Fig. 9) by the instrumented tower (Fig. 1) provide another means for evaluating the assimilation results. The tower sampled the low-level mesocyclone, main updraft, and rear-flank downdraft of the Arcadia storm (DB1997). Figure 9 illustrates the time series of tower measurements and EnKF model states at the tower location during the period when the mesocyclone and updraft passed the tower; samples of the dual-Doppler wind fields are also shown. The tower data in Fig. 9 are 5-min running averages. The 5-min length of the averaging window corresponds to the mean time between Doppler volume scans of the Arcadia storm. Since the storm was moving at 11 m s^{-1} , a 5-min average also corresponds to a sample over a 3.3-km distance in a storm-relative frame.

The Cimarron radar scans of the mesocyclone and updraft were toward the east and east-northeast. Therefore, the u component was observed well (although only above the level of the tower measurements that are shown). Perhaps not surprisingly, the u traces in the EnKF and dual-Doppler analyses follow the tower measurements rather closely (Fig. 9). The v component was mostly unobserved by the Cimarron radar, but the overall patterns in the EnKF and tower time series are still

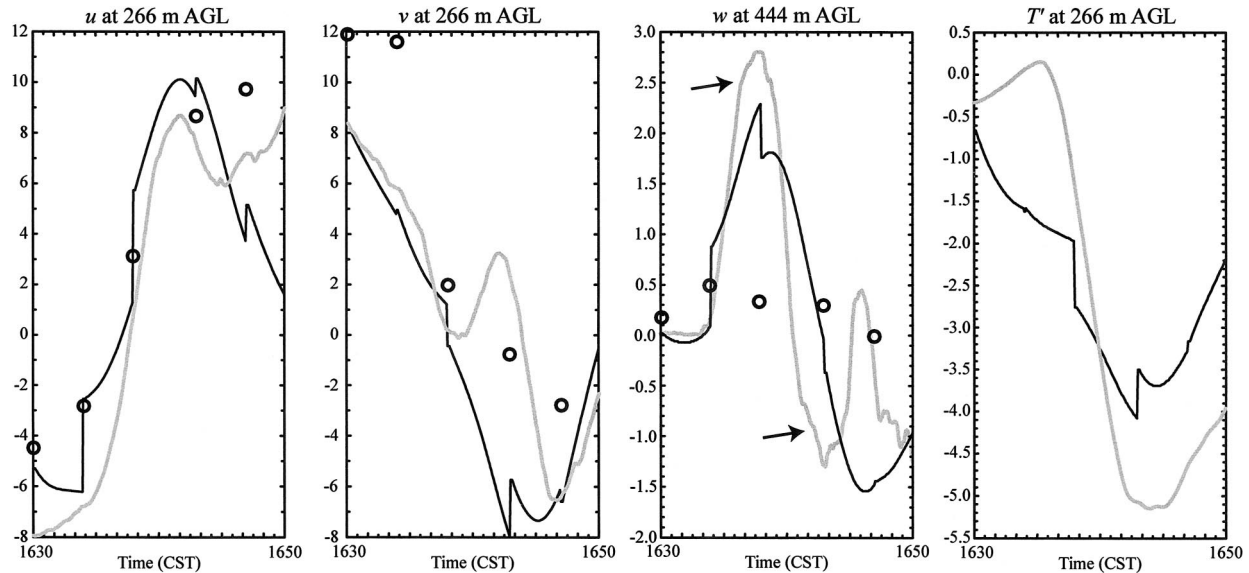


FIG. 9. Observations from the instrumented tower (5-min running averages, shown in gray) and corresponding traces of model-state variables in the control EnKF assimilation experiment at the tower location (black) between 1630 and 1650 CST. Samples from the dual-Doppler analysis are also shown (open circles). The analyzed fields, from left to right, are the westerly ground-relative wind component (u) at 266 m AGL (m s^{-1}), the southerly ground-relative wind component (v) at 266 m AGL (m s^{-1}), the vertical velocity (w) at 444 m AGL (m s^{-1}), and the perturbation temperature (T') at 266 m AGL (K). The arrows indicate the main updraft–downdraft couplet.

rather similar. The decrease in the v component before 1640 CST during the mesocyclone passage is retrieved particularly well. The values of v in the EnKF analyses are generally closer to the tower measurements than are the dual-Doppler values. After 1640 CST, there was an increase, then a sharp decrease, in v . The feature that produced this pattern in the tower measurements is indicated by neither the EnKF nor the dual-Doppler analysis.

A comparison of the vertical-velocity traces (Fig. 9) indicates that the EnKF analysis is considerably more accurate than the dual-Doppler analysis. The timing of the updraft maximum in the EnKF trace is the same as in the tower data, but the results suggest that the updraft in the EnKF analysis is too wide, and the transition from updraft to downdraft is too slow. Also, the temperature drop that occurs when the cold pool arrives is not sharp enough in the EnKF analysis, and the minimum temperature is not low enough. The differences in scale may be indicative of coarse model resolution.

Other information about EnKF performance is provided by comparison to other studies of the Arcadia storm (Weygandt et al. 2002a; Crook and Dowell 2003). Weygandt et al. (2002a; see their Fig. 4) applied a single-Doppler retrieval method to the Cimarron observations and obtained updraft strengths at 2.25 and 6.25 km at 1638 CST that our comparable to those in our study (Fig. 6); both the EnKF and single-Doppler algorithms processed three volumes of Cimarron radar data to obtain the analysis at 1638 CST. Since the EnKF and single-Doppler retrievals employed different grid resolu-

tions and data preprocessing methods, we will not attempt a more rigorous comparison.

A preliminary 4DVAR study of the Arcadia storm (Crook and Dowell 2003) employs the same numerical model, base state, and radar-data preprocessor as the current study. Qualitative analyses of the vertical-velocity fields and quantitative scores based on the retrieved cross-beam wind components indicate that the 4DVAR and EnKF methods are performing comparably, a result that has also been found in a comparison of 4DVAR and EnKF experiments using simulated observations (CSS). The 4DVAR analyses tend to be smoother than the EnKF analyses, probably because the former method includes temporal and spatial smoothness constraints in its formulation (Sun and Crook 1996). The results of both methods could probably be improved by reducing the impact of model error (Crook and Dowell 2003).

b. Sensitivity experiments

Since we are retrieving the atmospheric state in a mature storm by assimilating observations over a rather short period, the retrieved state is particularly sensitive to the ensemble-initialization procedure (SZ2003; Zhang et al. 2004). We initialized the control assimilation experiment by adding ellipsoidal perturbations in random locations to the base state over a 40 km wide and 12 km tall subdomain (section 2c). Instead, SZ2003 created ensemble members by adding random Gaussian noise to the base state. Figure 10a summarizes how alternative initializations similar to those proposed by

SZ2003 affect the assimilation results. Two experiments were initialized by adding to the base state random Gaussian noise with the following standard deviations: 5 m s^{-1} , 5 m s^{-1} , 5 K , 5 g kg^{-1} , and 5 g kg^{-1} for u , v , θ'_l , q_r , and q_t , respectively. These magnitudes are the same as those of the ellipsoidal perturbations in the control experiment. As in the control experiment, a correction procedure that eliminates negative mixing ratios was applied before integrating the ensemble members 20 min to the first observation time. In one experiment, we added random noise to only the 40-km-wide subdomain; in the other, we expanded the perturbation region horizontally to within 6 km of each lateral side of the domain.

The verification scores (on average, and at all but two of the verification times) indicate better retrievals in the control assimilation experiment than in the experiments with alternative initializations (Fig. 10a). One factor that affects EnKF performance is greater forecast spread at the observation points throughout the assimilation period in the control experiment than in either of the experiments initialized with random noise (not shown). Second, the experiments initialized with noise retain more small-scale structure than the control experiment; for example, after the initial 20-min integration, the strongest updrafts are narrower in the experiments initialized with noise than those in the control experiment (not shown). Third, the experiment initialized with Gaussian noise over most of the domain has more spurious cells, and these spurious cells have a negative impact on the ensemble mean, as discussed by SZ2003.

The assimilation results also depend on the model integration time between the initialization and the first observation time (Fig. 10b). We obtained slightly more accurate retrievals of the cross-beam winds before 1643 CST, and much more accurate retrievals after 1651 CST, by integrating the model for 20 min rather than for 5 or 10 min. The EnKF analysis at 1630 CST in the “20 min” experiment indicates a stronger upper-level updraft and more cloud water in the midlevel updraft than in the other experiments (not shown). Apparently, the 20-min experiment takes advantage of correlation structures representative of more mature storm cells (e.g., Fig. 3a) than the 5- or 10-min experiments. In addition, larger forecast spread in the 20-min experiment at 1630 CST means the first observation set has more impact on the analysis.

Since the quality of the retrieved azimuthal winds in all three experiments is nearly the same between 1643 and 1651 CST (Fig. 10b), the divergence of results after 1651 CST is unexpected. Further investigation reveals that the updraft nearly dissipates in the 5-min experiment during the model integration from 1651 to 1704 CST; in the 10-min experiment, the updraft weakens significantly, but not as much as in the 5-min experiment. Although the measures based on azimuthal winds between 1643 and 1651 CST (Fig. 10b) might suggest that the experiments have converged on the same so-

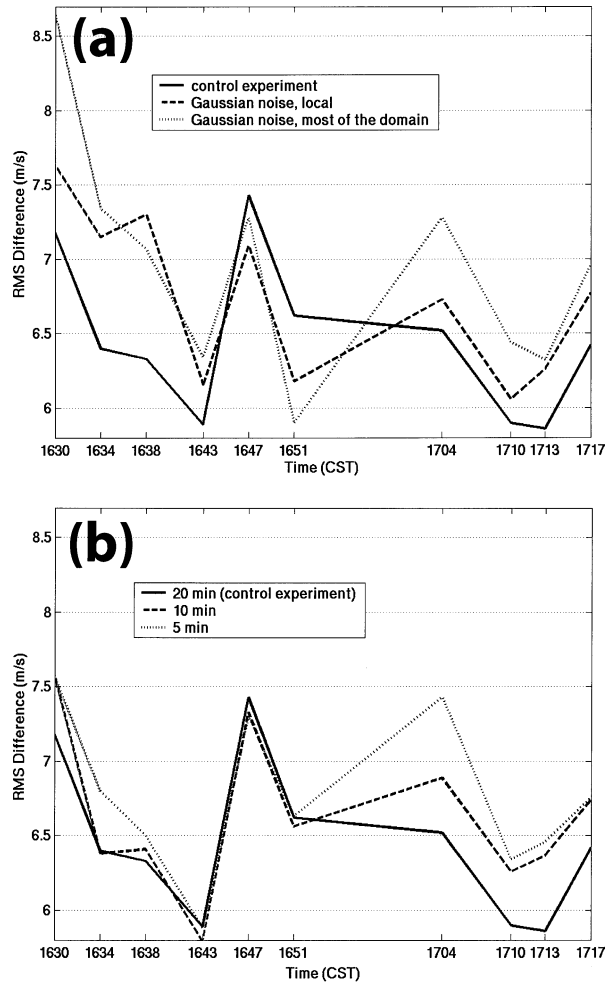


FIG. 10. Rms differences (m s^{-1}) between the azimuthal horizontal wind components in the dual-Doppler and EnKF analyses. Results are shown for experiments with different initializations. (a) Results for ensembles initialized with three different types of random perturbations: ellipsoidal perturbations added to a local (40 km wide) region (control assimilation experiment), Gaussian noise added to the same region, and Gaussian noise added to most of the domain. (b) Results for different periods of model integration before the assimilation of the first volume of Cimarron observations.

lution, analyses of other fields (not shown) indicate otherwise. For example, the warm anomaly in the midlevel updraft at 1651 CST is larger and stronger in the control experiment than in the 5- and 10-min cases.

Like SZ2003, we considered the value of retrieving unobserved thermodynamic fields by comparing the control assimilation experiment to an experiment in which the filter updates of θ'_l , q_r , and q_t were turned off during the processing of radial-velocity observations (Fig. 11). Only the velocity components u , v , and w were updated during the EnKF assimilation of radial velocity. The rainwater was still updated during the assimilation of reflectivity, as in the control experiment. The differences between the results of our two experiments are not nearly as great as those in similar “perfect

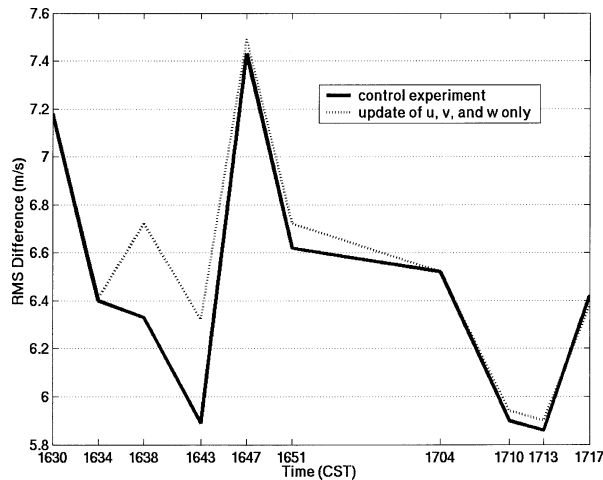


FIG. 11. As in Fig. 10, except the results of the control assimilation experiment are compared to those of one in which the filter updates of θ'_i , q_r , and q_t were turned off during the processing of radial velocity observations (i.e., radial velocity observations were used to update only u , v , and w).

model" experiments by SZ2003 (their Figs. 5 and 10). Nevertheless, the evidence indicates that the covariances between the velocity observations and the thermodynamic variables do provide some useful information that results in a more efficient retrieval early in the control experiment (Fig. 11). In our test, the results of both experiments eventually converged, and the retrievals of all fields are rather similar from 1647 CST on.

In the set of experiments summarized by Fig. 12, we varied the assumed standard deviation of radial-velocity observation errors (σ_{v_r}) from 1 to 4 m s⁻¹. Initially, smaller (larger) σ_{v_r} resulted in greater (lesser) fit to the observations, and more (less) accurate retrievals of the cross-beam winds. Later, the opposite was true; smaller (larger) σ_{v_r} tended to be associated with less (more) accurate retrievals. By the end of the assimilation period, the $\sigma_{v_r} = 1$ m s⁻¹ experiment had a very small ensemble spread. We conducted an additional experiment with the same observation-error variance but greater (10%) inflation; however, the cross-beam wind retrievals were slightly worse. Over the entire assimilation period, the accuracies of the retrieved winds in the $\sigma_{v_r} = 2, 3$, and 4 m s⁻¹ experiments are comparable, and the results of the $\sigma_{v_r} = 1$ m s⁻¹ experiment are somewhat worse.

In our final sensitivity experiments, we varied the radius of the influence region around each observation [i.e., the radius at which W in (1) and (2) drops to 0] from 2.0 to 10.0 km, keeping the influence region spherical in each case. To maintain approximately the same ensemble spread in each experiment, we specified the following inflation factors: no inflation in the 2.0-km experiment, 5% inflation in the 4.0- and 6.0-km experiments, 10% inflation in the 8.0-km experiment, and 15% inflation in the 10.0-km experiment. The differ-

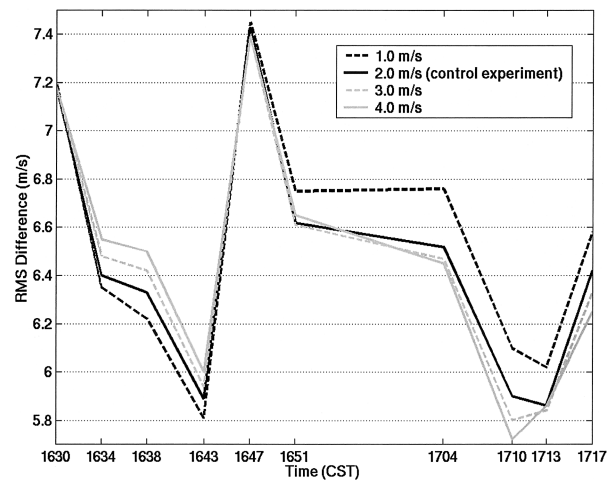


FIG. 12. As in Fig. 10, except the results of the control assimilation experiment are compared to those with different assumed magnitudes of radial-velocity observation error (σ_{v_r}).

ences in the results (Fig. 13) were most significant during the first half of the assimilation period, when larger (smaller) influence regions resulted in more (less) accurate retrievals of the cross-beam winds. Over the entire assimilation period, the retrieved winds in the 6.0- and 8.0-km experiments were the most accurate, but the retrieved fields were qualitatively similar in all the experiments in which the radius was 4.0 to 10.0 km. Similarly, SZ2003 noted that their results were rather insensitive to modest variations in the radius of the influence region about the optimal radius.

c. Higher-resolution assimilation experiment

Since the 2-km horizontal grid spacing in the control assimilation experiment is marginal for resolving some

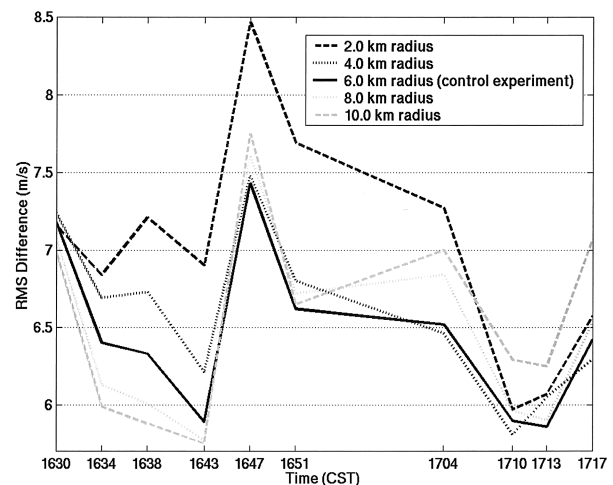


FIG. 13. As in Fig. 10, except the results of the control assimilation experiment are compared to those with different radii of the influence region around each observation.

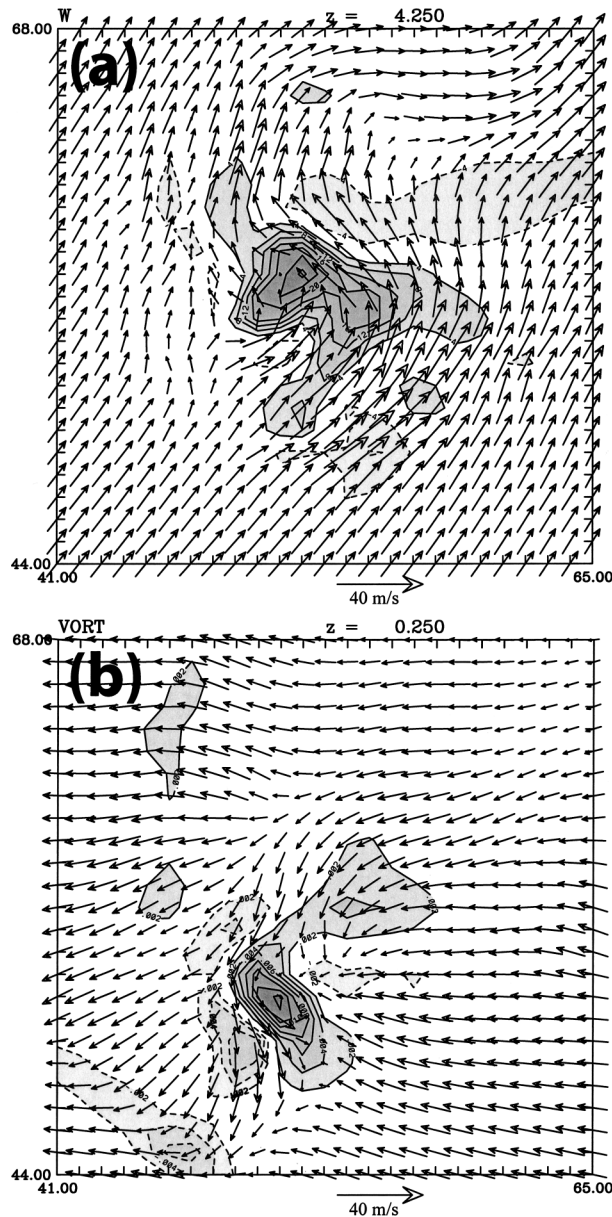


FIG. 14. EnKF analysis at 1704 CST in the higher-resolution assimilation experiment. The $24 \text{ km} \times 24 \text{ km}$ region that is shown corresponds to the dashed box in Figs. 7e, 7f, 8e, and 8f. (a) Vertical velocity (contours and shading at intervals of 4 m s^{-1}) and horizontal storm-relative winds (vectors) at 4.25 km AGL. (b) Vertical vorticity (contours and shading at intervals of 0.002 s^{-1}) and horizontal storm-relative winds (vectors) at 0.25 km AGL.

features in the Arcadia storm, we conducted an experiment with 1-km horizontal grid spacing. We prepared the observations for assimilation as before, except that we used a 500-m Cressman radius of influence to interpolate the observations to the finer grid. Since there are more objectively analyzed observations on the finer grid than on the coarser grid, we increased the inflation factor to 10% to compensate for the additional decrease in ensemble spread that results from assimilating more

observations. Otherwise, the assimilation method was the same as in the control assimilation experiment (section 2c).

The domain-averaged statistics for the higher-resolution experiment (not shown) indicate retrieval quality similar to that in the control experiment (Fig. 4). However, some individual storm features are apparently depicted more accurately in the higher-resolution assimilation experiment. The midlevel updraft in the EnKF analysis during the tornadic stage of the Arcadia storm is more curved in the higher-resolution experiment (Fig. 14a; cf. Fig. 7e), and the curved updraft surrounds a small rear-flank downdraft. These characteristics of the vertical-velocity field are more consistent with those in other tornadic storms (Lemon and Doswell 1979; Brandes 1984, his Figs. 8 and 17) and in simulated storms with strong vortices (Wicker and Wilhelmson 1995, their Fig. 12).

The higher-resolution assimilation experiment develops a much stronger and more realistic low-level vorticity maximum during the tornadic stage of the Arcadia storm (Fig. 14b; cf. Fig. 8e). The following features are all similar to those in the dual-Doppler analysis at low levels by DB1997 (their Fig. 10a): the curved region of cyclonic vorticity with an embedded maximum in its southern portion, the large region of anticyclonic vorticity along its western flank, and the small region of anticyclonic vorticity to the northeast of the vorticity maximum (Fig. 14b). However, there are still some problems in the low-level wind retrievals that are not solved by using the 1-km grid. A comparison of the dual-Doppler and EnKF analyses indicates that in the latter, low-level outflow that is too strong separates the low-level mesocyclone from the midlevel mesocyclone prematurely after 1704 CST (not shown).

The instrumented-tower and model traces indicate some benefit from higher resolution (Fig. 15; cf. Fig. 9). The vertical-velocity trace in the higher-resolution assimilation experiment is remarkably similar to that in the time-averaged tower data (second panel from right in Fig. 15), whereas the vertical velocity at the tower location decreased too slowly in the lower-resolution control experiment after the passage of the main updraft (Fig. 9). In addition, a more correct depiction of the rapid temperature drop before 1640 CST is indicated by the higher-resolution experiment. Although the scales of the main updraft, downdraft, and baroclinic zone are represented better in the higher-resolution experiment, there are still significant errors in the EnKF analyses. Curiously, the discrepancies between the tower and model traces for u are actually larger in the higher-resolution experiment than in the lower-resolution experiment (Figs. 9 and 15), and the rise and fall in v after 1640 CST are still not captured in the higher-resolution experiment (Fig. 15).

4. Temperature retrievals at low levels

For the reasons mentioned in the introduction, the characteristics of cold pools generated by evaporation

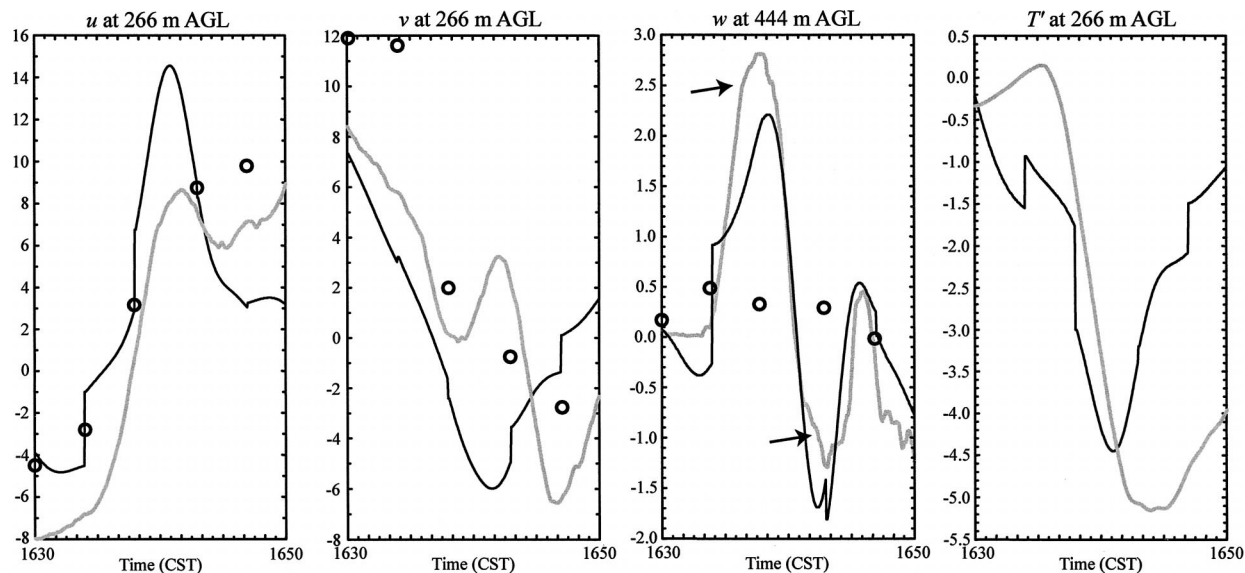


FIG. 15. As in Fig. 9, except for the higher-resolution assimilation experiment.

(or melting) of precipitation are of great interest in convective-storm research and forecasting. However, even mesonetworks of surface observations (e.g., Brock et al. 1995) are unable to resolve the storm-scale structures of surface cold pools. Since the density of radar measurements in convective storms is significantly greater than the density of in situ temperature measurements, there have been many attempts to deduce temperature from radar data (e.g., Hane et al. 1981; Brandes 1984; Roux 1985; Ziegler 1985; Sun and Crook 1998). Unfortunately, retrieving temperature from real radar data is often difficult, especially near the surface. For example, Brandes (1984) retrieved the wind and temperature fields in two tornadic storms observed by the Oklahoma dual-Doppler radar system; then, he analyzed the baroclinic generation of horizontal vorticity in parcels approaching the low-level mesocyclone. The analyses indicated vorticity generation of opposite signs in the two cases, suggesting that either the storm dynamics in the two cases were actually different, or the retrieved fields were not accurate enough for one to analyze baroclinic generation even in a qualitative sense. Possible explanations for poor temperature retrievals from Doppler data include infrequent volumetric scanning, that is, the inability to estimate velocity time tendencies (Gal-Chen and Kropfli 1984; Crook 1994), and poor spatial resolution near the ground.

The results of three experiments help demonstrate how the cold pool develops in the Arcadia simulation and how it is affected by assimilation of observations. The first is the control assimilation experiment, described in section 2c. The second assimilation experiment, described previously in section 3b, is the one in which the filter updates of θ'_i , q_i , and q_i were turned off during the processing of radial-velocity observations. A third assimilation experiment was initialized

with the results of an idealized simulation. In the same model used for the assimilation experiments, we initiated convection in the idealized simulation by adding a 2-K warm bubble at low levels to an otherwise homogeneous base state. After 4200 s of model integration (without assimilation), the velocity fields in the idealized simulation attained their best fit to the 1630 CST Cimarron observations. (We determined the best overall fit by computing differences between the observed and simulated radial winds every 5 min in the model, accounting for differences in storm locations by horizontally shifting the model fields by integer numbers of grid points until the best fit was obtained at each time.) The assimilation was then accomplished according to the following procedure: 1) generate an ensemble by adding perturbations, which have the same characteristics as those used to initialize the control assimilation experiment, to the model fields at 3900 s in the idealized simulation, 2) integrate the ensemble for 300 s, 3) assimilate the 1630 CST Cimarron volume, and 4) implement the procedure described in section 2c for integrating the ensemble and assimilating the remaining radar data.

The results of the control assimilation experiment and the new assimilation experiment initialized with the idealized simulation are quite different (Figs. 16, 17a, and 17b), even though the same observations were assimilated in the same way in each case. Initializing the assimilation procedure with an idealized simulation does improve the retrieval of cross-beam wind components by over 0.5 m s^{-1} at the first time but actually results in worse retrievals by up to 1.5 m s^{-1} at later times (Fig. 16a). Perhaps more importantly, even though the same observations were assimilated, the results of the experiments with different initializations diverged rather than converged. The differences in the experiments are

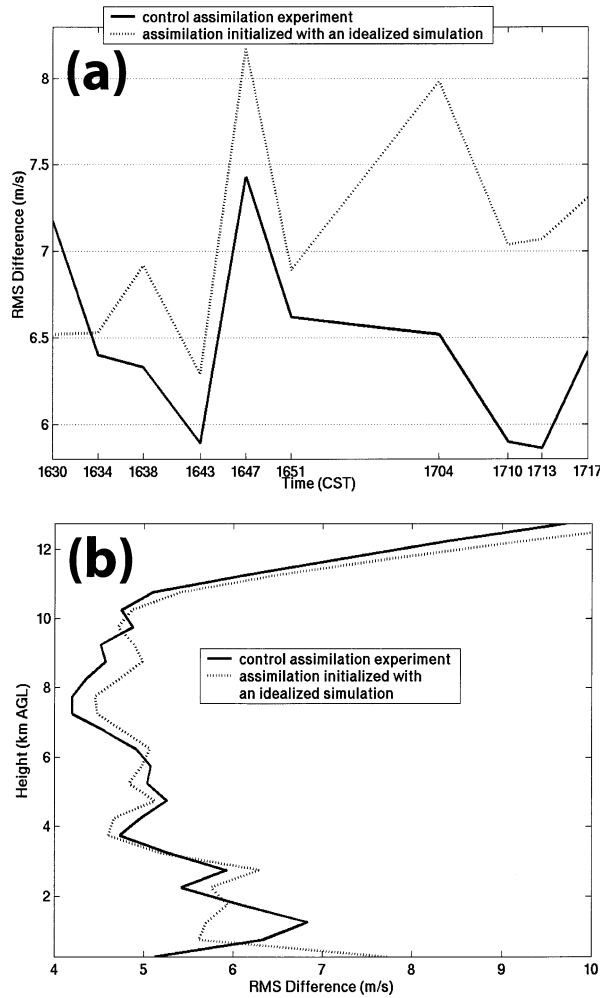


FIG. 16. Rms differences (m s^{-1}) between the azimuthal horizontal wind components in the dual-Doppler analyses and those in the ensemble-mean states of two assimilation experiments: the control experiment and an experiment that was initialized with the results of an idealized simulation. (a) Domain-averaged statistics as a function of time. (b) Statistics as a function of height, averaged over four times (1638, 1643, 1647, and 1651 CST).

particularly large in the lowest 1.5 km AGL (Fig. 16b), which motivates our focus on the low-level features.

The analysis at 1638 CST in the assimilation experiment initialized with the idealized simulation (Fig. 17b) illustrates a problem that developed eventually in all assimilation experiments. Specifically, erroneous northerly storm-relative winds developed in the location of the observed mesocyclone (Fig. 17b; cf. observations 4 min earlier in Fig. 8b), and the retrieved vorticity maximum was 7 km from the observed location. The large region of northerly outflow was associated with a cold pool that was stronger than in the control experiment, both in terms of the minimum temperature perturbation (-6.2 K versus -4.5 K) and the areal coverage of cold temperatures (Figs. 17a and 17b). A similar outflow problem developed later in the control assimilation ex-

periment; by 1704 CST, strong storm-relative winds from the northeast had developed along the storm's forward flank, and the retrieved low-level mesocyclone was too weak and displaced too far southwest (section 3a; cf. Figs. 8e and 8f). Although the temperature minima at the tower location in the two assimilation experiments are both within about 1 K of the observed minimum (Figs. 9 and 18), neither experiment's temperature trace represents well the observed trace. For example, cooling at the tower location began too soon in both experiments.

The assimilation experiments indicate that the cold-pool characteristics are primarily a function of the integrated effect of evaporative cooling in the model rather than a result of assimilating velocity observations. In the control experiment, the development of a coherent precipitation core in the ensemble mean began with the assimilation of reflectivity observations in the first data volume. Therefore, the characteristics of the cold pool at 1638 CST (Fig. 17a) represent the cumulative effect of evaporation of rain in the model for 8 min. In the assimilation initialized with the idealized simulation, a cold pool was already present at the time of the first data assimilation. Rainwater started to reach the surface and a cold pool began to develop in the idealized simulation approximately 30 min before the start of the assimilation period. Therefore, by 1638 CST (Fig. 17b), the cold pool had been strengthening and expanding over a period of nearly 40 min.

Relative to evaporative cooling in the model, assimilating velocity observations had only a minor impact on the cold pools. A significant low-level cold pool developed in the model whether the filter was used to retrieve temperature (Fig. 17a) or was not (Fig. 17c). Between 1630 and 1638 CST, the filter did lower the temperature somewhat near the southern end of the cold pool (Fig. 17d), but the net effect of the filter was relatively minor. In the assimilation experiment initialized with the idealized simulation, in which the temperature was too low at the lower location early in the assimilation period, Doppler-velocity assimilation correctly produced warming there at 1634 and 1638 CST, but the magnitudes of the corrections were much too small (Fig. 18).

We speculate that observational limitations help explain why the cold pool was poorly retrieved from the Doppler-velocity measurements. The divergence signature associated with the cold pool was probably too shallow to be documented by the Doppler observations owing to the beamwidth and radar-horizon constraints. Even when the mesocyclone of the Arcadia storm was only 25 km from the Cimarron radar, the lowest radar observations were still a few 100 m AGL, which was probably not low enough (DB1997). In addition, the lack of useful radial-velocity observations in clear air could have been a problem in this case; the wind field in the trailing cold pool, outside the precipitation region, was not resolved. To summarize, the failure to retrieve

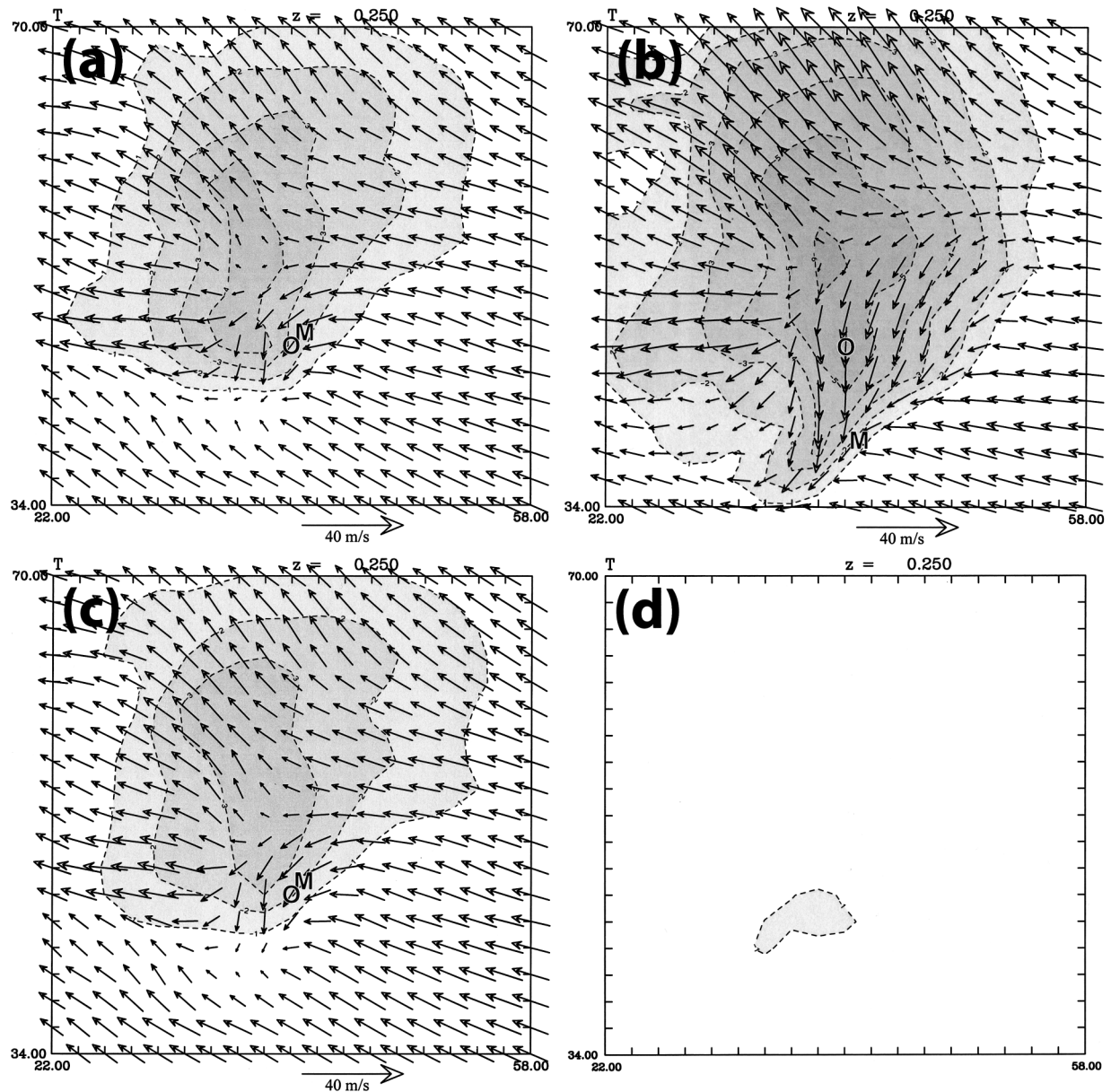


FIG. 17. Perturbation temperature (contours and shading at intervals of 1 K) and horizontal storm-relative winds (vectors) at 0.25 km AGL in a 36 km \times 36 km region at 1638 CST. Here, “O” and “M” indicate the locations of the vertical vorticity maxima in the observations and model, respectively. (a) Ensemble mean in the control assimilation experiment. (b) Ensemble mean in the assimilation initialized with an idealized simulation. (c) Ensemble mean in the assimilation experiment in which the filter updates of θ_i , q_i , and q_i were turned off. (d) Sum of the filter increments of temperature at 1630, 1634, and 1638 CST in the control assimilation experiment (winds not shown).

the cold pool is likely attributed to weak covariances between low-level temperature and the available Doppler observations because these observations did not cover critical regions in the storm. The difficulties in retrieving temperature from Doppler observations in our experiments are analogous to those reported by Weygandt et al. (2002b), who applied a traditional temperature-retrieval method to the Arcadia data. Weygandt et al. noted that a cold pool was “conspicuously absent” in their retrieved fields.

It is also likely that model deficiencies limited the extent to which the cold-pool characteristics could be recovered from the observations. First, the coarse model grid, particularly the 500-m vertical grid spacing, might have been insufficient to represent the cold-pool structure. Second, uncertainties in parameterizations of moist processes were probably significant error sources in our experiments. The precipitation scheme in the model does not include ice, but we know the Arcadia storm produced significant amounts of hail (DB1997).

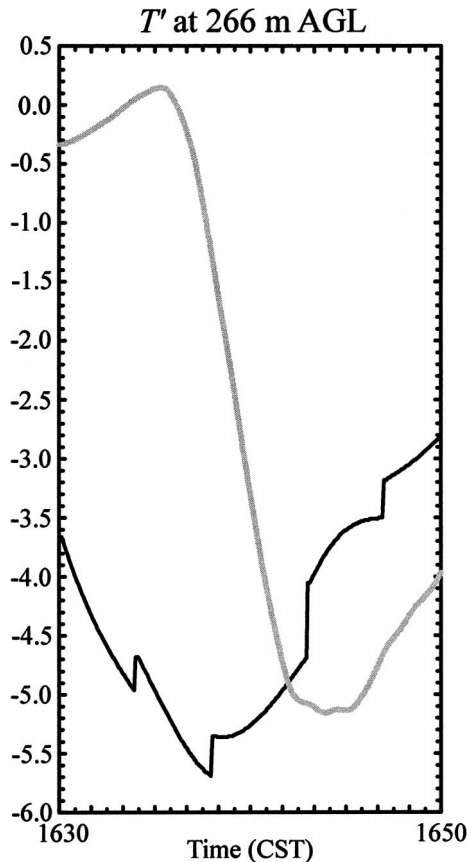


FIG. 18. As in Fig. 9, except for the assimilation experiment initialized with the idealized simulation. Only the analyses of perturbation temperature are shown.

5. Conclusions

The feasibility of retrieving the wind and temperature fields in an observed supercell storm was tested by applying an ensemble Kalman filter to observations of radial velocity and reflectivity from a single Doppler radar. The EnKF data assimilation algorithm processed 10 observation volumes of the mature 17 May 1981 Arcadia, Oklahoma, storm over a period of 47 min. A comparison of the EnKF assimilation results to all available observations indicates that the locations of the retrieved main updraft and mesocyclone were generally correct. Furthermore, the strengths of these features were comparable to what could be obtained by a dual-Doppler analysis of observations at the same resolution. Most of the improvement in the retrieved wind fields occurred during the assimilation of the first two data volumes.

Retrievals of all fields were particularly sensitive to the method of producing the initial ensemble. Reasonable changes in other assimilation parameters, including the inflation factor and the assumed magnitude of the radial velocity observation error, had relatively minor impacts on the results. Results were poor when the radius of the influence region around each observation

was only 2 km; better results were obtained by employing radii in the range of 4–10 km.

Assuming all observations in each volume were collected simultaneously simplified the observation processing and the verification in these experiments. Better results could probably be obtained by assimilating observations at the actual times when they were collected (Sun and Crook 1998). Better use of reflectivity information could also lead to better results. Assimilating the low values of reflectivity outside the precipitation core, which was not considered in this study, could be one way to damp spurious cells that develop in the ensemble members. The effects of spurious cells in these experiments were subtle but could be more significant in other case studies.

A more challenging but potentially rewarding avenue for improving the results would be to refine the model and/or use an adaptive assimilation method that attempts to account for model error (e.g., Mitchell and Houtekamer 2000). Increasing the horizontal resolution in one of the tests was an effort to reduce model error in these experiments and did improve the analyses of some fields. Uncertainties in parameterizations of moist processes are particularly significant sources of error in attempts to simulate observed convective storms. The current experiments employed a warm-rain scheme, whereas the abundance of hail produced by the Arcadia storm indicates that ice species were important. Errors in the microphysical scheme probably contributed to poor forecasts of the low-level cold pool in these experiments.

A series of experiments indicates that assimilating Doppler-velocity observations had relatively little impact on the gross characteristics of the low-level cold pool. We speculate that the velocity “signature” of the cold pool was shallow and was below the lowest Doppler scans. Instead, the cold pool in the Arcadia assimilation was retrieved indirectly in that it developed primarily as a result of model processes (evaporation of rain) in regions where the reflectivity observations indicated precipitation. Since the evolution of convection over periods of tens of minutes depends significantly on cold pools, the implications for operational numerical forecasting of convection are discouraging if cold pools cannot be predicted well by the model, and assimilation of Doppler observations cannot correct the model trajectory. In the future, we hope to determine what additional information (e.g., higher-resolution Doppler data with better clear-air sensitivity, dual-polarization observations that provide more information about microphysical parameters, and more dense networks of surface observations) will be required to obtain more accurate retrievals of low-level cold pools.

Acknowledgments. This research was supported by the Advanced Study Program at the National Center for Atmospheric Research (NCAR), by the United States Weather Research Program, and by National Science

Foundation Grants 0205655 and 0205599. This study would not have been possible without the assistance of Jenny Sun and Bill Skamarock. We appreciate reviews of the manuscript by Alain Caya, David Stensrud, and three anonymous reviewers. Conversations with Steve Weygandt and Jeff Anderson were also quite helpful.

REFERENCES

- Anderson, J. L., and S. L. Anderson, 1999: A Monte Carlo implementation of the nonlinear filtering problem to produce ensemble assimilations and forecasts. *Mon. Wea. Rev.*, **127**, 2741–2758.
- Armijo, L., 1969: A theory for the determination of wind and precipitation velocities with Doppler radars. *J. Atmos. Sci.*, **26**, 570–573.
- Brandes, E. A., 1984: Relationships between radar-derived thermodynamic variables and tornadogenesis. *Mon. Wea. Rev.*, **112**, 1033–1052.
- Brock, F. V., K. C. Crawford, R. L. Elliott, G. W. Cuperus, S. J. Stadler, H. L. Johnson, and M. D. Eilts, 1995: The Oklahoma Mesonet: A technical overview. *J. Atmos. Oceanic Technol.*, **12**, 5–19.
- Carbone, R. E., M. J. Carpenter, and C. D. Burghart, 1985: Doppler radar sampling limitations in convective storms. *J. Atmos. Oceanic Technol.*, **2**, 357–361.
- Cressman, G. P., 1959: An operational objective analysis system. *Mon. Wea. Rev.*, **87**, 367–374.
- Crook, A., 1994: Numerical simulations initialized with radar-derived winds. Part I: Simulated data experiments. *Mon. Wea. Rev.*, **122**, 1189–1203.
- Crook, N. A., 1996: Sensitivity of convection initiation to low-level thermodynamic fields. *Mon. Wea. Rev.*, **124**, 1767–1785.
- , and D. Dowell, 2003: Assimilating radar observations of a supercell storm into a cloudscale model: 4DVar and ensemble Kalman filter results. Preprints, *31st Conf. on Radar Meteorology*, Seattle, WA, Amer. Meteor. Soc., 154–157.
- Dee, D. P., 1995: On-line estimation of error covariance parameters for atmospheric data assimilation. *Mon. Wea. Rev.*, **123**, 1128–1145.
- Doviak, R. J., P. S. Ray, R. G. Strauch, and L. J. Miller, 1976: Error estimation in wind fields derived from dual-Doppler radar measurement. *J. Appl. Meteor.*, **15**, 868–878.
- Dowell, D. C., and H. B. Bluestein, 1997: The Arcadia, Oklahoma, storm of 17 May 1981: Analysis of a supercell during tornadogenesis. *Mon. Wea. Rev.*, **125**, 2562–2582.
- Droegemeier, K. K., and R. B. Wilhelmson, 1985: Three-dimensional numerical modeling of convection produced by interacting thunderstorm outflows. Part I: Control simulation and low-level moisture values. *J. Atmos. Sci.*, **42**, 2381–2403.
- Evensen, G., 1994: Sequential data assimilation with a nonlinear quasi-geostrophic model using Monte-Carlo methods to forecast error statistics. *J. Geophys. Res.*, **99** (C5), 10 143–10 162.
- Foote, G. B., and P. S. duToit, 1969: Terminal velocity of raindrops aloft. *J. Appl. Meteor.*, **8**, 249–253.
- Gal-Chen, T., 1978: A method for the initialization of the anelastic equations: Implications for matching models with observations. *Mon. Wea. Rev.*, **106**, 587–606.
- , 1982: Errors in fixed and moving frame of references: Applications for conventional and Doppler radar analysis. *J. Atmos. Sci.*, **39**, 2279–2300.
- , and R. A. Kropfli, 1984: Buoyancy and pressure perturbations derived from dual-Doppler radar observations of the planetary boundary layer: Applications for matching models with observations. *J. Atmos. Sci.*, **41**, 3007–3020.
- Gaspari, G., and S. E. Cohn, 1999: Construction of correlation functions in two and three dimensions. *Quart. J. Roy. Meteor. Soc.*, **125**, 723–757.
- Hamill, T. M., 2001: Interpretation of rank histograms for verifying ensemble forecasts. *Mon. Wea. Rev.*, **129**, 550–560.
- , J. S. Whitaker, and C. Snyder, 2001: Distance-dependent filtering of background error covariance estimates in an ensemble Kalman filter. *Mon. Wea. Rev.*, **129**, 2776–2790.
- Hane, C. E., and P. S. Ray, 1985: Pressure and buoyancy fields derived from Doppler radar data in a tornadic thunderstorm. *J. Atmos. Sci.*, **42**, 18–35.
- , R. B. Wilhelmson, and T. Gal-Chen, 1981: Retrieval of thermodynamic variables within deep convective clouds: Experiments in three dimensions. *Mon. Wea. Rev.*, **109**, 564–576.
- Houtekamer, P. L., and H. L. Mitchell, 1998: Data assimilation using an ensemble Kalman filter technique. *Mon. Wea. Rev.*, **126**, 796–811.
- , and —, 2001: A sequential ensemble Kalman filter for atmospheric data assimilation. *Mon. Wea. Rev.*, **129**, 123–137.
- Joss, J., and A. Waldvogel, 1970: Raindrop size distribution and Doppler velocities. Preprints, *14th Conf. on Radar Meteorology*, Tucson, AZ, Amer. Meteor. Soc., 153–156.
- Kalman, R. E., 1960: A new approach to linear filtering and prediction problems. *J. Basic Eng.*, **82D**, 35–45.
- Kapitzka, H., 1991: Numerical experiments with the adjoint of a non-hydrostatic mesoscale model. *Mon. Wea. Rev.*, **119**, 2993–3011.
- Laroche, S., and I. Zawadzki, 1994: A variational analysis method for retrieval of three-dimensional wind field from single-Doppler radar data. *J. Atmos. Sci.*, **51**, 2664–2682.
- Lemon, L. R., and C. A. Doswell III, 1979: Severe thunderstorm evolution and mesocyclone structure as related to tornadogenesis. *Mon. Wea. Rev.*, **107**, 1184–1197.
- Lilly, D. K., 1990: Numerical prediction of thunderstorms—Has its time come? *Quart. J. Roy. Meteor. Soc.*, **116**, 779–798.
- Mitchell, H. L., and P. L. Houtekamer, 2000: An adaptive ensemble Kalman filter. *Mon. Wea. Rev.*, **128**, 416–433.
- , —, and G. Pellerin, 2002: Ensemble size, balance, and model-error representation in an ensemble Kalman filter. *Mon. Wea. Rev.*, **130**, 2791–2808.
- Ray, P. S., C. L. Ziegler, W. Bumgarner, and R. L. Serafin, 1980: Single- and multiple-Doppler radar observations of tornadic storms. *Mon. Wea. Rev.*, **108**, 1607–1625.
- Rotunno, R., and J. Klemp, 1985: On the rotation and propagation of simulated supercell thunderstorms. *J. Atmos. Sci.*, **42**, 271–292.
- , —, and M. L. Weisman, 1988: A theory for strong, long-lived squall lines. *J. Atmos. Sci.*, **45**, 463–485.
- Roux, F., 1985: Retrieval of thermodynamic fields from multiple-Doppler radar using the equations of motion and the thermodynamic equation. *Mon. Wea. Rev.*, **113**, 2142–2157.
- Rutledge, S. A., and P. V. Hobbs, 1983: The mesoscale and microscale structure and organization of clouds and precipitation in a mid-latitude cyclone. VIII: A model for the “seeder-feeder” process in warm-frontal rainbands. *J. Atmos. Sci.*, **40**, 1185–1206.
- Scialom, G., and Y. Lemaitre, 1990: A new analysis for the retrieval of three-dimensional mesoscale wind fields from multiple Doppler radar. *J. Atmos. Oceanic Technol.*, **7**, 640–665.
- Shapiro, A., S. Ellis, and J. Shaw, 1995: Single-Doppler velocity retrievals with Phoenix II data: Clear air and microburst wind retrievals in the planetary boundary layer. *J. Atmos. Sci.*, **52**, 1265–1287.
- Snyder, C., and F. Zhang, 2003: Assimilation of simulated Doppler radar observations with an ensemble Kalman filter. *Mon. Wea. Rev.*, **131**, 1663–1677.
- Sun, J., and N. A. Crook, 1994: Wind and thermodynamic retrieval from single-Doppler measurements of a gust front observed during Phoenix II. *Mon. Wea. Rev.*, **122**, 1075–1091.
- , and —, 1996: Comparison of thermodynamic retrieval by the adjoint method with the traditional retrieval method. *Mon. Wea. Rev.*, **124**, 308–324.
- , and —, 1997: Dynamical and microphysical retrieval from Doppler radar observations using a cloud model and its adjoint.

- Part I: Model development and simulated data experiments. *J. Atmos. Sci.*, **54**, 1642–1661.
- , and —, 1998: Dynamical and microphysical retrieval from Doppler radar observations using a cloud model and its adjoint. Part II: Retrieval experiments of an observed Florida convective storm. *J. Atmos. Sci.*, **55**, 835–852.
- , and —, 2001: Real-time low-level wind and temperature analysis using single WSR-88D data. *Wea. Forecasting*, **16**, 117–132.
- , D. W. Flicker, and D. K. Lilly, 1991: Recovery of three-dimensional wind and temperature fields from simulated single-Doppler radar data. *J. Atmos. Sci.*, **48**, 876–890.
- , N. A. Crook, and J. Miller, 2001: Assimilation and forecasting of a supercell storm: Simulated and observed data experiments. Preprints, *30th Int. Conf. on Radar Meteorology*, Munich, Germany, Amer. Meteor. Soc., 188–190.
- Taylor, W. L., Ed., 1982: 1981 spring program summary. NOAA Tech. Memo. ERL NSSL-93, 97 pp.
- Thorpe, A. J., M. J. Miller, and M. W. Moncrieff, 1982: Two-dimensional convection in nonconstant shear: A model of mid-latitude squall lines. *Quart. J. Roy. Meteor. Soc.*, **108**, 739–762.
- van Leeuwen, P. J., 1999: Comments on “Data assimilation using an ensemble Kalman filter technique.” *Mon. Wea. Rev.*, **127**, 1374–1377.
- Weisman, M. L., and J. B. Klemp, 1984: The structure and classification of numerically simulated convective storms in directionally varying wind shears. *Mon. Wea. Rev.*, **112**, 2479–2498.
- Weygandt, S. S., A. Shapiro, and K. K. Droegemeier, 2002a: Retrieval of model initial fields from single-Doppler observations of a supercell thunderstorm. Part I: Single-Doppler velocity retrieval. *Mon. Wea. Rev.*, **130**, 433–453.
- , —, and —, 2002b: Retrieval of model initial fields from single-Doppler observations of a supercell thunderstorm. Part II: Thermodynamic retrieval and numerical prediction. *Mon. Wea. Rev.*, **130**, 454–476.
- Whitaker, J. S., and T. M. Hamill, 2002: Ensemble data assimilation without perturbed observations. *Mon. Wea. Rev.*, **130**, 1913–1924.
- Wicker, L. J., and R. B. Wilhelmson, 1995: Simulation and analysis of tornado development and decay within a three-dimensional supercell thunderstorm. *J. Atmos. Sci.*, **52**, 2675–2703.
- Wu, B., J. Verlinde, and J. Sun, 2000: Dynamical and microphysical retrievals from Doppler radar observations of a deep convective cloud. *J. Atmos. Sci.*, **57**, 262–283.
- Xu, Q., C.-J. Qiu, and J.-X. Yu, 1994: Adjoint-method retrievals of low-altitude wind fields from single-Doppler wind data. *J. Atmos. Oceanic Technol.*, **11**, 579–585.
- , L. Wang, and K. Nai, 2003: Error covariance estimation for Doppler wind data assimilation. Preprints, *31st Conf. on Radar Meteorology*, Seattle, WA, Amer. Meteor. Soc., 108–109.
- Zhang, F., C. Snyder, and J. Sun, 2004: Impacts of initial estimate and observation availability on convective-scale data assimilation with an ensemble Kalman filter. *Mon. Wea. Rev.*, **132**, 1238–1253.
- Ziegler, C. L., 1985: Retrieval of thermal and microphysical variables in observed convective storms. Part I: Model development and preliminary testing. *J. Atmos. Sci.*, **42**, 1487–1509.